THE DEVELOPMENT OF A SKELETAL MUSCLE BIO-ACTUATOR USING 3-D STEREOLITHOGRAPHY

BY

CAROLINE ELIZABETH CVETKOVIC

THESIS

Submitted in partial fulfillment of the requirements
for the degree of Master of Science in Bioengineering
in the Graduate College of the
University of Illinois at Urbana-Champaign, 2013

Urbana, Illinois

Adviser:

Professor Rashid Bashir

ABSTRACT

Over the past decade, a new scientific discipline has emerged, integrating mechanics with biology to create complex engineered living systems. The building blocks – different cell types in an instructive environment – can be assembled in various ways to promote the emergence (or natural evolution and interaction) of the cells in a system with well-defined functionality. These functions could include sensing, information processing, protein expression, and actuation, among countless others.

This Thesis presents a novel cellular system capable of actuation and fabricated using cells and hydrogels. A stereolithographic 3D printing technique (SLA) was used to create a hydrogel backbone made of a beam connecting two pillars that supports a muscle strip created from skeletal muscle cells in a fibrin-based matrix. The entire device is termed a "bio-bot," or biological robot. Contraction of the cells within the muscle strip produced enough force to move the pillars and displace the bio-bot on a surface in a liquid medium. This Thesis is focused on the development and characterization (mechanical and biological) of the skeletal muscle-based biological actuator.

The use of the SLA allowed for easy modifications of the polymerized part's geometry and material properties. Increasing the energy dose of polymerization produced a stiffer beam that restricted bending and increased the passive tension in the muscle strip. 15-19 days after cell seeding, the bio-bots displayed spontaneous contraction that resulted in a net displacement of up to ~6 mm in 10 minutes. During this time span, a maximum velocity of over 1890 μm/min was achieved. Future plans are focused on controlling the activity of the bio-bot using optogenetics.

ACKNOWLEDGEMENTS

I dedicate this Thesis to all of those who have helped me to achieve this important milestone in my academic career.

I would like to thank my adviser, Prof. Rashid Bashir, for the motivation and support of my project, as well as the opportunity to pursue my interests in your lab group. Many thanks to Dr. Vincent Chan for the much-valued mentorship, training, guidance, and encouragement you have given me. Thank you to Ritu Raman for your assistance with the mechanical characterization and simulations. I would also like to recognize my colleagues in the LIBNA group, especially Dr. Brian Dorvel and Elise Corbin, for your encouragement and incredible willingness to help.

I am grateful for the funding provided by the National Science Foundation Science and Technology Center, 'Emergent Behaviors of Integrated Cellular Systems' (EBICS, Grant 0939511), as well as the National Science Foundation Integrative Graduate Education and Research Traineeship, 'Training the Next Generation of Researchers in Cellular and Molecular Mechanics and BioNanotechnology' (CMMB IGERT, Grant 0965918). This support has transformed my education at the University of Illinois from a possibility to a reality. Thank you also to Mike Poellman, Sarah Holton, Prof. Taher Saif, and Dr. Mayandi (Shiv) Sivaguru at UIUC, and to Dr. Mahmut Selman Sakar and Prof. Harry Asada at MIT, for your help with various aspects of the project.

Finally, I would like to acknowledge my family and friends, whose unconditional support has been very much appreciated throughout all of my educational pursuits. Thank you.

TABLE OF CONTENTS

1. INTRODUCTION

1.1 OVERVIEW AND SIGNIFICANCE

Over the past decade, a new scientific discipline has emerged, integrating mechanics with biology to create complex engineered living systems. The building blocks – different cell types in an instructive environment – can be assembled in various ways to promote the emergence (or natural evolution and interaction) of the cells in a system with well-defined functionality. These functions could include sensing, information processing, protein expression, and actuation (**Figure 1.1**).

Scientists at the forefront of this research envision the extent of cellular and biological systems to include devices that are able to sense their surroundings and perform accordingly. Kamm *et al.* provide numerous examples of the cellular systems that can have real-world implications in medicine and the environment:

- a biological "robot" or organism that has the ability to recognize a chemical gradient and produce a response, such as moving towards an oil spill for environmental remediation or neutralizing a dangerous toxin within the body;
- an engineered "organ" to sense drug and protein levels or glucose concentration in the bloodstream and send the information to a feedback loop or insulin pump;
- a micro-fluidic system acting as a human organ platform (heart, lung, or liver to eliminate harmful and costly drug development and testing; and
- plants with neurons that can send out a signal for water or nutrients after sensing a local deficiency.

All of these – and countless more – could potentially be achieved with the use of a few cell types, specifically neurons, endothelial cells, and muscle cells, which can be differentiated from stem cells (Kamm et al., 2010).

This Thesis presents a novel cellular system capable of actuation and fabricated using cells and hydrogels. A stereolithographic 3D printing technique was used to create a hydrogel backbone made of a beam connecting two pillars that supports a muscle strip made of skeletal muscle cells in a fibrin-based matrix. The entire device is termed a "bio-bot," or biological robot. Contraction of the cells within the muscle strip produced enough force to move the pillars and displace the bio-bot on a surface in a liquid medium. This Thesis is focused on the development and characterization (mechanical and biological) of the skeletal muscle-based biological actuator. Future plans are focused on controlling the activity of the bio-bot using optogenetics.

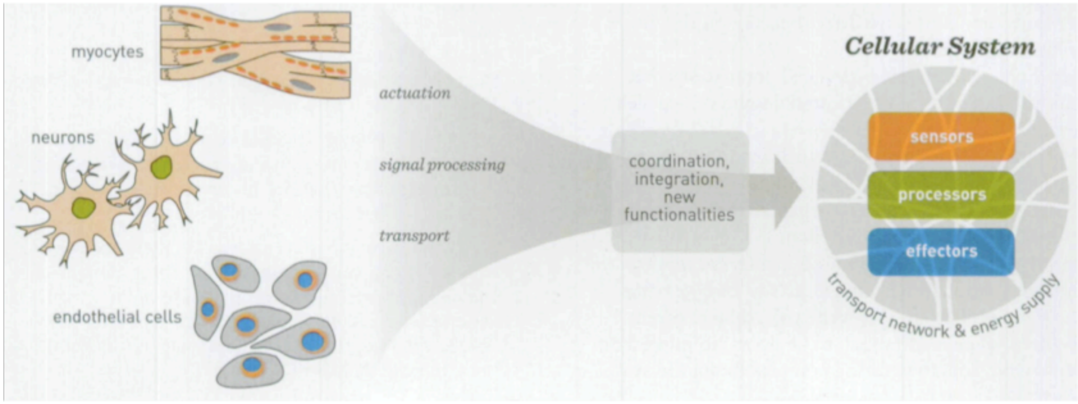

Figure 1.1: A Cellular System. Different cell types integrate and coordinate to form a cellular system (Kamm et al., 2010)

1.2 SPECIFIC AIMS

- *Specific Aim 1*: To engineer an autonomous, 3-dimensional biological actuator (bio-bot) using stereolithography.
- *Specific Aim 2*: To optimize the design and performance of the device with biological and mechanical characterization of the bio-bot and muscle strip.
- *Specific Aim 3*: To achieve net locomotion of the bio-bot.

1.3 ORGANIZATION OF THESIS

This Thesis is organized as follows: *Chapter 1* presents an overview, a discussion on the emergence of cellular systems, and a review of the Specific Aims. *Chapter 2* provides a broad literature review of the topics most relevant to this work: biological machines, 3D stereolithography, fibrin biomaterials, and skeletal muscle engineering. *Chapter 3* outlines the protocols and materials used to carry out the aspects of this study, including fabrication, mechanical testing, cell culture, formation of the muscle strip, immunofluorescent analysis, and analysis of actuation. *Chapter 4* presents the results of this study and offers a thoughtful discussion and analysis. *Chapter 5* discusses potential future directions for the project and offers a broader perspective.

2. BACKGROUND AND LITERATURE REVIEW

2.1 BIOLOGICAL MACHINES

Biological machines are cellular systems with the ability to perform work. They exist on all length scales, from an ATP synthase or a DNA replication enzyme, to a kinesin molecule walking along a microtubule, or an organ such as the kidney functioning as a factory. The 17-century life scientist Marcello Malpighi described nature's way of operating the body as creating "a very large number of machines, which are of necessity made up of extremely minute parts so shaped and situated, such as to form a marvelous organ…" (Piccolino, 2000). Other scientists of this pre-industrial age adopted a similar view of the body's physiological functions and mechanics being guided by principles similar to those driving man-made machines. Just as a machine in a factory required an energy source, a bodily machine was prompted into action by chemical, electrical, or mechanical stimuli. Scientists of today's era have built on these notions to engineer a class of biological machines using cellular and molecular building blocks.

2.1.1 SINGLE-MOLECULE AND SINGLE-CELL BIOLOGICAL MACHINES

Bio-motors powered by molecules such as ATPase and kinesin have been used to transport actin filaments, microtubules, and micro posts (Clemmens et al., 2004; Noji et al., 1997; Soong et al., 2000). However, based on previous reports, a generated force greater than a few pN per molecule is not to be expected (Fisher & Kolomeisky, 1999). Biological machines driven by a few or a sheet of living cells can produce a greater force than that of molecular motors. Their mechanical properties can be exploited to produce actuation or fluid movement (with forces ranging from nano-Newtons to micro-Newtons) without the need for an exogenous energy source (Tanaka et al., 2007a).

Simpler biological machines harness the power of one or a few cells such as microorganisms and cardiomyocytes. Itoh and colleagues used an electric potential gradient to control the motion of protozoa. *Paramecium* were directed to move objects through a culture medium with an output force of about 27 nN (Itoh, 2000). A unicellular photosynthetic algae guided by visible light (*Chlamydomonas reinhardtii)* produced enough power to transport 3 μm beads through a fluid with a velocity of over 100 μm/s

(Weibel et al., 2005). Finally, Hiratsuka *et al*. created a micro-motor by guiding bacteria along a circular track to spin a rotor (Hiratsuka et al., 2006).

Morishima and colleagues created a micro-actuator that exploited the contraction of a few cardiomyocytes to displace arrays of hydrogel micro-pillars in a contractile force measurement system. The cellular machine was powered with exogenous glucose instead of electrical energy stimulus to bend the RGDS-coated PDMS pillars a maximum of 6 μm with a force of only 80 pN (Morishima et al., 2006). Additionally, Kim and Park created a "hybrid cell motor" capable of actuating a micro-rotor by contractile forces of a few cardiomyocytes seeded in polymer micro-wells, with each producing an average force of 20 μN/well (Kim et al., 2006). However, movement of a larger structure or self-powered autonomous device demands a higher force production and consequently a greater number of cells. Thus, the majority of biological machines are driven with a cluster or sheet of cells.

2.1.2 BIOLOGICAL PUMPS

One variety of biological machines is a pump that produces enough energy to move fluid, much as a heart valve or swimming organism can do. Tung *et al*. tethered a small number of flagellar motors to magnetic micro-beads and copper coils to generate AC power at about 1 mW/L. This system was also used as a microfluidic pump that employed the rotation of the tethered cells to produce a "fluidic conveyor belt" to move liquid across a channel (Tung & Kim, 2006). Many bio-actuating pumps have used cardiomyocyte sheets, which synchronously contract to produce a force. Tanaka *et al*. created a "pump on a microchip" in which cell sheet pulsation produced an oscillatory fluid motion within a micro-channel (Tanaka et al., 2006). This concept was expanded to create a micro-spherical heart pump by surrounding a hollow sphere containing inlet and outlet ports with a cardiomyocyte cell sheet. As the cells contracted around the elastic sphere, capillary fluid motion in the cell culture medium became oscillatory with a heart-like pumping motion that did not require a wired or electrical connection (Tanaka et al., 2007b). Feinberg and colleagues altered the shape and thickness PDMS-based thin films to create machines that displayed pumping characteristics (**Figure 2.1A**). A coiled-spring actuator oscillated between systolic (rolled) and diastolic (loosely coiled) states in response to the cyclic contraction of the cardiomyocytes. Another structure resembling a helical paper towel tube was capable of extension and rotation, prompting the authors to propose a “simple suction mode micro-pump.” Finally, an arched thin film was seeded with cardiomyocytes on its concave surface to form a gripping device (Feinberg et al., 2007). Nawroth, Feinberg, Parker and colleagues also demonstrated the successful reverse engineering of a jellyfish-like structure (termed a “medusoid”, **Figure 2.1D**) that acted as a muscle-based pump. A jellyfish proved to be an ideal model for such a demonstration, as only a few cell types, including muscle cells and motor neurons, are necessary for actuation (Nawroth et al., 2012).

2.1.3 MUSCLE-BASED BIOLOGICAL ACTUATORS

The advantages of using muscle cells (cardiac or skeletal) for biological machines are numerous. First, unlike traditional machines that require an external energy source, these cells can be powered with glucose and other ions or biomolecules. Additionally, muscle cells instinctively respond to mechanical forces and displacements of their environments. The ability to sense and quickly adapt to cues and applied stimuli is both a characteristic of muscular tissues and a requirement for higher-order biological machines. Cardiomyocytes in particular are able to self-synchronize through electrical communication (Pilarek et al., 2011). Muscle performs almost silently, and the waste produced from the conversion of biochemical fuel to mechanical waste is biodegradable (Dennis & Herr, 2005). Finally, a muscle cell can produce a higher force of contraction than another type of cell or micro-organism. As a motor, muscle can efficiently produce a workload of 1000 Joules for every 1 gram of consumed glucose (Herr & Dennis, 2004). Many other synthetic actuating devices are unable to perform similarly and cannot achieve the same range of sizes and forms that muscle tissue can.

Some engineered actuators naturally evolved from constrained structures to freestanding devices capable of net displacement. Xi and colleagues integrated a silicon-based microelectromechanical system (MEMS) cantilever device with a sacrificial thermally responsive polymer, poly-N-isopropylacrylamide (PNIPAAm), over which cardiac cells were seeded. By allowing the cells to adhere to specified locations and create anisotropic patterns guided by the chemistry of the surface, they permitted the components to ‘self-assemble’ into a functional system. A system with cantilevers of different lengths was used to analyze the mechanical properties of muscle cells as their contraction (power stroke) displaced the cantilevers in a repeated manner. Mobile and autonomous devices were also released, using the MEMS-based thin film structure as a backbone that the muscle bundle could bend to produce forward movement (**Figure 2.1C**). The maximum observed velocity was 236 μm/s with an average frequency of 1.8 Hz (Xi et al., 2005).

Feinberg *et al.* created centimeter-scale, cardiomyocyte-based “biohybrid muscular thin films” that were engineered to perform various tasks (swimming and walking) based on a micro-base that was able to spontaneously achieve a specific shape. The machines harnessed energy from a combination of the unique structure-function relationship of the PDMS material and its geometric and mechanical properties. When the various 2D PDMS films were released from a PIPAAm-coated glass cover slip, they accepted different 3D conformations that varied depending on PDMS thickness, stiffness, and temperature. The degree of isotropy of the 2D myocardium dictated contractility, and observed specific forces were comparable to those of native cardiac tissue. The walking “myopod” maintained a velocity of 133 μm/s with electrical stimulation, while the triangular swimmer moved with an average speed of 30 μm/s (Feinberg et al., 2007).

Perhaps the most efficient pathway to creating a functional bio-actuator has been to mimic nature’s own work. Kim and colleagues designed a “crab-like micro-robot” consisting of three PDMS legs connected to a central body, upon which cardiomyocytes adhered and contracted to produce net displacement over a ten-day period (**Figure 2.1B**). The grooved, fibronectin-coated backbone allowed for greater mechanical output of the cardiac cells. Asymmetry from the variance of leg lengths provided the key geometric factor for net motion with an observed average velocity of 100 μm/s (Kim et al., 2007). Although the fabrication technology allowed for mass production of devices, molding is a time consuming process that is limited in terms of materials.

A more recent biological actuator from Chan and colleagues produced net motion but was manufactured with a simpler, faster, and more flexible fabrication system. Building on previous work demonstrating the use of 3D stereolithography to create a multi-material cantilever of poly(ethylene glycol) diacrylate (PEGDA) and acrylic-PEG-collagen, the researchers created a millimeter-scale "bio-bot" that not only mimicked the native myocardium in terms of elasticity, but also was able to move upon a surface in fluid (**Figure 2.1E**). A sheet of cardiomyocytes seeded on top of the bimorph cantilever contracted to induce a power stroke that moved the bio-bot forward with an average beating frequency of 1.5 Hz and a maximum velocity of 236 μm/s, resulting in a net displacement of approximately one body length in 30 seconds (Chan et al., 2012).

In addition to devices with the ability to "walk" or "crawl", various machines have been designed to move through a body of fluid without surface contact by mimicking water-based organisms. Herr and Dennis created a swimming biological robot with frog semitendinosus muscles that was able to start, stop, turn, and swim in a straight line at over 1/3 body lengths per second. However, this "bio-mechanotronic" design was integrated with an embedded micro-controller, and could not swim without this stimulation (Herr & Dennis, 2004). As described earlier, Nawroth's medusoids (millimeter-scale muscle-elastomer bilayers) were composed of rat cardiomyocytes and a thin layer of PDMS in an open-bell shape with eight radiating lobes. When electrical field stimulation was applied to the fluid, the medusoids responded in a way that mimicked the swimming and feeding mechanisms of the real organism, achieving velocities of 0.4-0.7 body lengths per stroke (Nawroth et al., 2012).

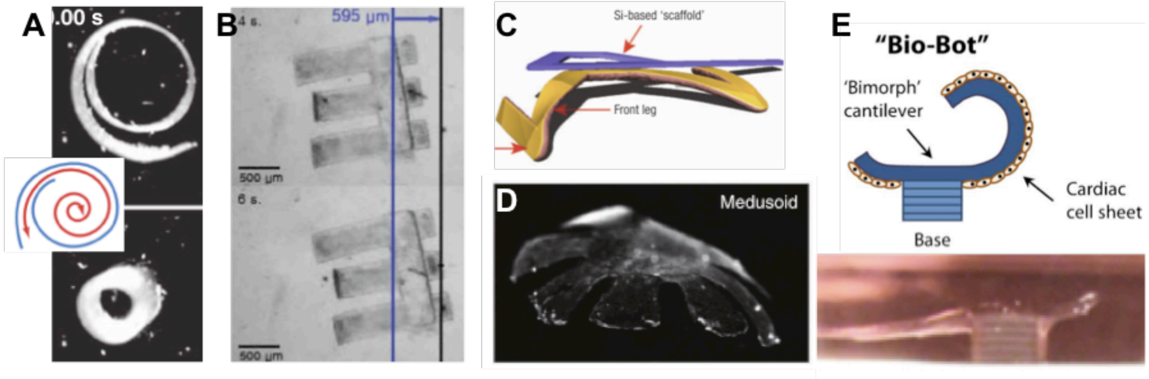

Figure 2.1: Engineered Biological Actuators. (A) A coiled muscular thin film (Feinberg et al., 2007) (B) Biohybrid crab-like micro-robots (J. Kim et al., 2007) (C) A self-assembled micro-device driven by muscle power (Xi et al., 2005) (D) Medusoid actuator resembling a jellyfish (Nawroth et al., 2012) (E) "Walking" cantilever bio-bot (Chan et al., 2012)

2.2 STEREOLITHOGRAPHY

2.2.1 FUNDAMENTALS OF STEREOLITHOGRAPHY

Stereolithography is a liquid-based rapid prototyping technology that uses a light source to build a computer-designed part in an additive, layer-by-layer fashion. It was the first solid freeform fabrication technique to be commercially available in the mid-1980s (Melchels et al., 2010). Since then, it has been used for a wide range of applications on different size scales.

The basic operation of a stereolithography apparatus (SLA) involves five steps: creation of a computer-aided design (CAD) model (or equivalent design), conversion into a tessellated (.stl) file, slicing into parallel horizontal layers, preparation of polymerization specifications (layer thickness, building style, cure depth, and hatch spacing), and finally, building. During this last step, a laser beam is focused at the surface of the material and controlled by a computer to directly trace a pattern onto the surface of a resin, a liquid material that has the ability to solidify rapidly upon exposure to light. The energy of the photon must be greater or equal to the energy difference between the ground and excited states for the resin material. When the material absorbs adequate energy, reactive species are produced and chemical cross-linking occurs via an exothermic process (Bártolo, 2011; Jacobs, 1992). After the resin is polymerized to a certain depth, the platform is lowered a specified distance, the object is re-coated with resin (either manually if the resin is held in a container on the platform, or automatically by lowering the platform into a vat of liquid resin), and the laser polymerizes the second layer, continuing in this manner until all layers are completed (**Figure 2.2**). Adherence to the previous layer is ensured by the fact that the laser penetrates deeper than the specific layer thickness to cure some unpolymerized groups from the first layer (Cho & Kang, 2012; Melchels et al., 2010).

The laser is a continuous beam of solid, liquid, or gaseous form that is sent through a beam-expanding telescope and series of scanning mirrors. In a gas laser, the laser head contains a discharge tube that determines the laser's performance characteristics by providing an optical gain, the heat exchanger dissipates wasted heat generated in the laser tube, and the power supply excites and regulates the electrical current. In a helium cadmium (HeCd) laser (which uses a wavelength of 325 nm and power around 40 mW), neutral helium atoms are excited to a metastable state and can then collide with neutral cadmium atoms, causing an excitation state from which both visible and ultraviolet (UV) light propagates (Jacobs, 1992). The smallest possible feature is dictated by the laser beam diameter, which is typically 250 μm but can be as low as 75 μm in high-resolution systems. Because the laser scans the surface of the resin, the horizontal precision is about equal to half of the width of the beam. Maximum power density is achieved at the focal point of the lens (i.e., the location of minimum beam diameter) (Arcaute et al., 2011; Bártolo, 2011; Bertsch & Renaud, 2011).

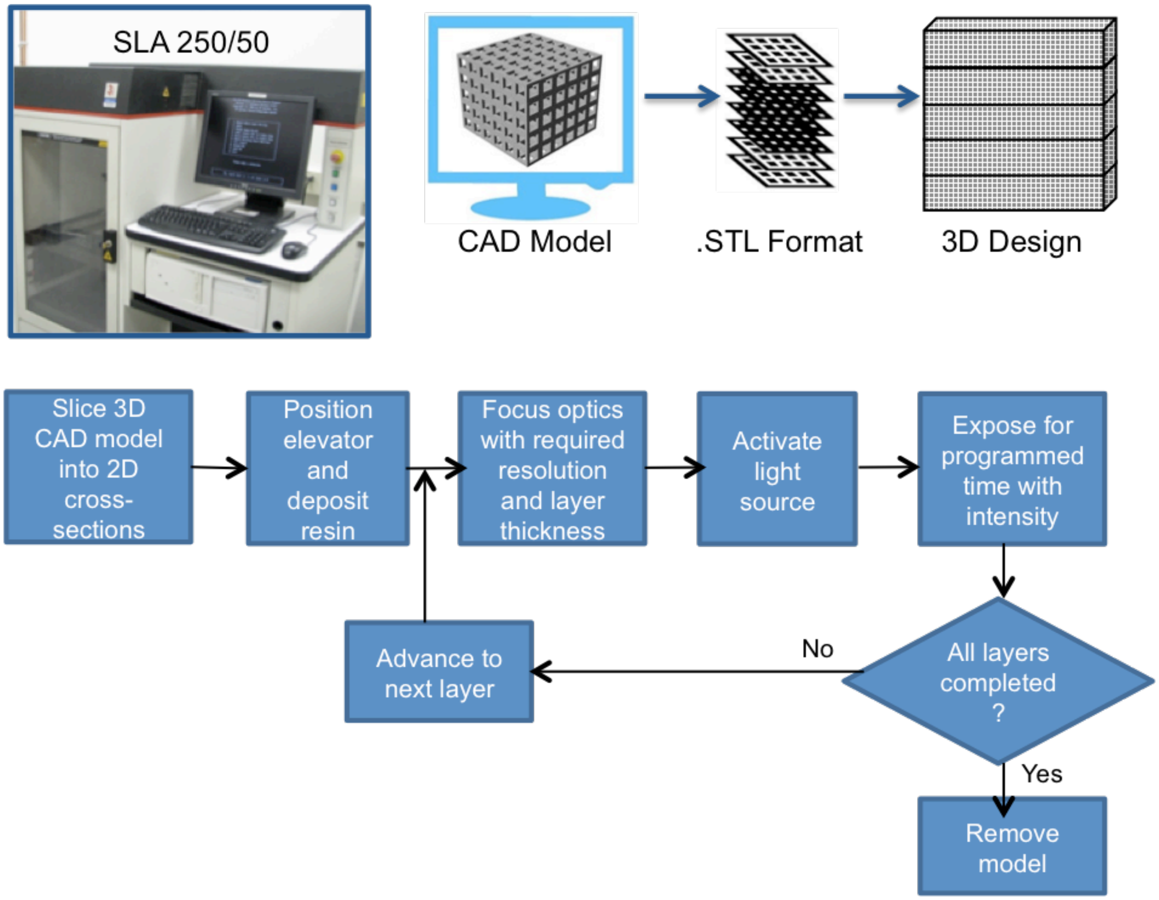

Figure 2.2: Stereolithography Flow Process. Adapted from (Melchels et al., 2010)

Polymerization is achieved through the use of a photoinitiator (PI) in the pre-polymer solution that reacts with photons from the UV light to produce free radicals. These catalytic radical species propagate through the material to chemically link monomer units into larger polymer chains in a process that includes initiation, propagation, and termination. The time of polymerization is dependent on the responsiveness and the surface tension of the photopolymer, speed of the scanning mirrors, and power and wavelength of the laser (Jacobs, 1992).

A "Working Curve" equation is derived from the Beer-Lambert Law, which describes the intensity of light's exponential decay as it travels through an absorbing medium. The equation quantifies the relationship between the maximum exposure (E_{max}), the critical energy dose needed to polymerize the material from a liquid to a solid gel state (E_C), the thickness or cure depth (C_D), and the penetration depth (D_P) of the laser into the material:

$$C_D = D_P \cdot \ln\left(\frac{E_{max}}{E_C}\right)$$

The critical energy dose needed to solidify the resin depends on the photoinitiator concentration and amount of dissolved oxygen as well as other inhibiting species in the local environment. The equation is valid within a cure depth range of $D_P < C_D < 4D_P$ (Jacobs, 1992). This Working Curve relationship between energy and thickness (for different materials) can be used to create design parameters for fabricated structures.

The application dictates the material choice. Tissue engineering scaffolds should eventually be able to degrade, whereas materials for bone defects, dental implants, vascular stents, and other medical applications should maintain mechanical and structural integrity over time. Depending on the material, when the fabricated object is placed in a solvent, swelling can occur. Distortion of the structure can result, demonstrating the importance of material choice (Cho & Kang, 2012). Certain polymer units, such as vinyl acrylate monomers with a carboxylic (-COOH) group and carbon-carbon double bonds, are more reactive than others. Chemical modification of the material before polymerization can result in different post-fabrication material properties (Jacobs, 1992).

2.2.2 BIOMEDICAL APPLICATIONS OF STEREOLITHOGRAPHY

Over the past few decades, stereolithography has been used increasingly for biomedical applications. For example, Gibson *et al*. detailed the use of rapid prototyping technology for medical models: image data obtained from a patient's CT, MRI, or ultrasound scans can be converted to an appropriate format using medical software and then used to aid the surgeon in diagnosis, pre-operative planning, and models of body parts or implants based on the exact specifications of the patient's needs (Gibson et al., 2006). Other uses of stereolithography for medical purposes have included oral and maxillofacial surgery, where the natural bone or tissue is modeled and reconstructed for cosmetic and functional applications; artificial joints (knees, hips, and articular joints); nerve guidance channels; surgical tools for complex surgeries; printing of avascular organs (such as ears and aortas); and customized implants such as hearing aids (Boland et al., 2007; Melchels et al., 2010). However, because the smallest feature size is regulated by the specifications of the system and spot size of the laser, the minimum resolution is a limiting factor for accuracy in medical applications (Gibson et al., 2006; Peltola et al., 2008).

2.2.2.1 STEREOLITHOGRAPHY FOR TISSUE ENGINEERING

Tissue engineering is the creation of functional organs and tissues for the repair or replacement of injured or diseased body parts (Peltola et al., 2008). It combines a biocompatible material with cells, biomolecules, and growth factors in a supportive scaffold, matrix, or gel system. Most tissue-engineered systems must be able to support cell proliferation and migration in a spatially distributed manner. The 3D micro-environment offers mechanical support, a nutrient supply, and cell adhesion to mimic the native extracellular matrix (ECM). Complex pore geometry is difficult to achieve with conventional assembly methods; for this reason, stereolithography can be used to rapidly fabricate a scaffold or system with controllable geometric and mechanical properties on both the micro- and macro- scales. It has the advantage of being able to polymerize a range of biomaterials with varying degrees of degradability (Cho & Kang, 2012).

2.2.2.2 CELL ENCAPSULATION AND ALIGNMENT WITH POLYMERIZED HYDROGELS

Hydrogels are a widely used biomaterial because of their mechanical resemblance to native ECM tissue and ability to be chemically and biologically modified for use with cells and proteins. Dhariwala and colleagues were the first to demonstrate successful encapsulation of cells using SLA technology. They polymerized 3D rings of poly(ethylene oxide) (PEO) and poly(ethylene glycol) dimethacrylate (PEGDMA) hydrogels with Chinese hamster ovary (CHO-B2) cells. Cytotoxicity was evaluated as a function of PI concentration, with an average of 64% live cells after 3 days in culture (Dhariwala et al., 2004). Others soon established encapsulation methods for other cell types such as fibroblasts and marrow stromal cells, with many cells exhibiting better post-fabrication viability with the incorporation of RGD (Arg-Gly-Asp) peptides (Lu et al., 2006; Melchels et al., 2010).

Arcaute, Mann, and Wicker first used stereolithography to polymerize photoreactive PEGDMA (M_W 1000) structures with encapsulated cells. A study of the polymerized cure depths based on pre-polymer concentrations and applied energy dose was used to find the optimal conditions for long-term encapsulation within the centimeter-scale gel disks. They demonstrated 87% viability of dermal fibroblasts after 24 hours, with no significant decrease during the two hours following fabrication. Additionally, they demonstrated that increasing the concentration of PI also increased cytotoxicity – a concern when working with living cells. A PI concentration less than 0.5% was recommended for long-term studies (Arcaute et al., 2006, 2011). These results were used to create multi-material, PEG-based scaffolds with polymerized bio-active domains for specific cell adhesion, as cells will not attach to inert PEG hydrogels (Arcaute et al., 2010).

Chan *et al.* encapsulated NIH/3T3 fibroblasts in polymerized PEGDA hydrogels of different molecular weights (M_W 700, 3400, and 5000, representing a range of physiologically relevant stiffness values from 5-500 kPa). Higher molecular weights increased the swelling ratio (and pore size) of the hydrogel, but decreased the elastic modulus. The highest relative cell viability after 14 days (quantified by MTS assay) was observed with PEG M_W 3400 chemically linked with RGDS peptides. Cells were also labeled with different fluorescent dyes to demonstrate multi-layer patterning capabilities of the SLA (Chan et al., 2010). This study was extended to include the encapsulation C2C12 muscle cells, PC12 neuron-like cells, primary hippocampal neurons, and adipose-derived stem cells in various PEG-based materials. The study allowed for the examination of cellular interactions as well as the influence of spatial organization and regulation defined by the SLA (Bajaj et al., 2012; Zorlutuna et al., 2011).

Jeong, Chan, and colleagues encapsulated NIH/3T3 fibroblasts into a fabricated "microvascular stamp" made of permeable PEGDA-MA (methacrylic alginate) hydrogels. The cells were induced to secrete pro-angiogenic growth factors that localized within the cylindrical channels of the circular stamp. When the stamp was implanted on an embryonic chick chorioallantoic membrane (CAM), neovessels sprouted and formed in the pattern of pre-defined features. The SLA easily produced stamps with different pattern geometries; a channel diameter of 500 μm resulted in the greatest quantity of functional neovessels *in vivo* (Jeong et al., 2012). This group also demonstrated the use of the SLA in combination with micro-contact printing (μCP) to pattern cell alignment on 3D hydrogels with ECM proteins. They used a polydimethylsiloxane (PDMS) stamp to apply acryl-fibronectin protein "ink" to a glass coverslip, on top of which a PEGDA hydrogel was polymerized. The construct was inverted and seeded with NIH/3T3 cells that adhered to the protein domains. The width of the patterned acryl-fibronectin lines was altered in order to maximally align the cells (Chan et al., 2012).

2.2.3 OTHER RAPID PROTOTYPING TECHNOLOGIES

Other rapid prototyping technologies allowing for layer-by-layer fabrication can be liquid-based (two-photon polymerization), solid-based (fused deposition modeling), or powder-based (selective laser sintering and 3D printing). These methods are favored because of their relative speed when compared to other traditional fabrication techniques such as molding or casting (Melchels et al., 2010). However, in comparison to other rapid prototyping techniques, the relative ease of iterations, enhanced visualization capabilities, lower cost and cycle time, short time frame from idea conception to physical part, and ability to cure a wide range of materials and photopolymers make stereolithography a more attractive technology with a myriad of biomedical applications.

2.3 FIBRIN AS A BIOMATERIAL

2.3.1 FIBRIN STRUCTURE, POLYMERIZATION, AND MECHANICAL PROPERTIES

Fibrin is a hydrogel with a 3D branching fiber network. The fibrin monomer is made from the cleavage of fibrinogen, a 45 nm long glycoprotein comprised of polypeptide chains, by the enzyme thrombin. Thrombin is a proteolytic enzyme that selectively cleaves fibrinopeptides at the Arg-Gly residues in the central region on the fibrinogen molecule, and is activated by the cleavage of prothrombin in response to injury or foreign surfaces (Weisel, 2005). *In vitro*, a specific quantity or concentration of thrombin is added to fibrinogen, which initiates the fibrin clotting process; *in vivo*, the process is dynamic and the thrombin concentration changes during the course of the reaction, depending on local conditions (Wolberg, 2007).

The removal of the fibrinopeptides (which prevent spontaneous polymerization) exposes specific binding sites that result in half-staggered arrangement and lateral aggregation of fibrin protofibrils. The fibrin monomers that result can combine into staggered two-stranded protofibrils, which aggregate laterally to form twisted fibers (**Figure 2.3**). When energy of bonding is exceeded by the energy required to stretch an additional protofibril, lateral growth of the fiber terminates. As protofibrils diverge, fibers can be branched into a 3D network, with the majority of branches consisting of an intersection of three fibers. Branching is essential for fibrin to become a space-filling hydrogel material. The material is soluble as a fibrinogen monomer but insoluble as a fibrin gel. Factor XIIIa is a transglutaminase (activated by thrombin) that stabilizes the clot from mechanical, chemical, and proteolytic harm. It forms a covalent bond between the lysine resides from one fibrin molecule and the glutamine resides in another molecule (Ryan et al., 1999; Weisel, 2005, 2007). In general, fibrin polymerizes relatively quickly when compared to other ECM proteins such as collagen and laminin, an intuitive feature considering the prominent role that fibrin plays in blood clotting and wound repair *in vivo* (Janmey et al., 2009).

Mechanically, fibrin filaments are relatively ‘soft’ compared to other filamentous biomaterials. The elastic modulus of a fibrin strand has been measured to within 1.5-10 MPa, which is less than that of actin and microtubules (Collet et al., 2005). The individual fibers comprise a low volume fraction of the polymer and can undergo large deformations without breaking; it has been shown that fibers can strain up to 120% without any evident damage from the extension (Liu et al., 2006).

Fibrin is a viscoelastic material, displaying properties of an elastic solid, in which deformation is proportional to applied stress and independent of strain rate, as well as a viscous liquid, where stress is proportional to strain rate but independent of deformation itself (Weisel, 2007). Its viscoelastic mechanical properties are closely linked to function; *in vivo*, a fibrin blood clot must be able to respond to and withstand blood flow pressure and have the strength to stop blood flow (Weisel, 2004). Its mechanical properties, which are those of native connective tissue, make fibrin a useful scaffold material for the engineering of cartilage, nerve tissue, and cardiovascular tissue; however, it does not exhibit sufficient mechanical strength for bone repair applications (Janmey et al., 2009).

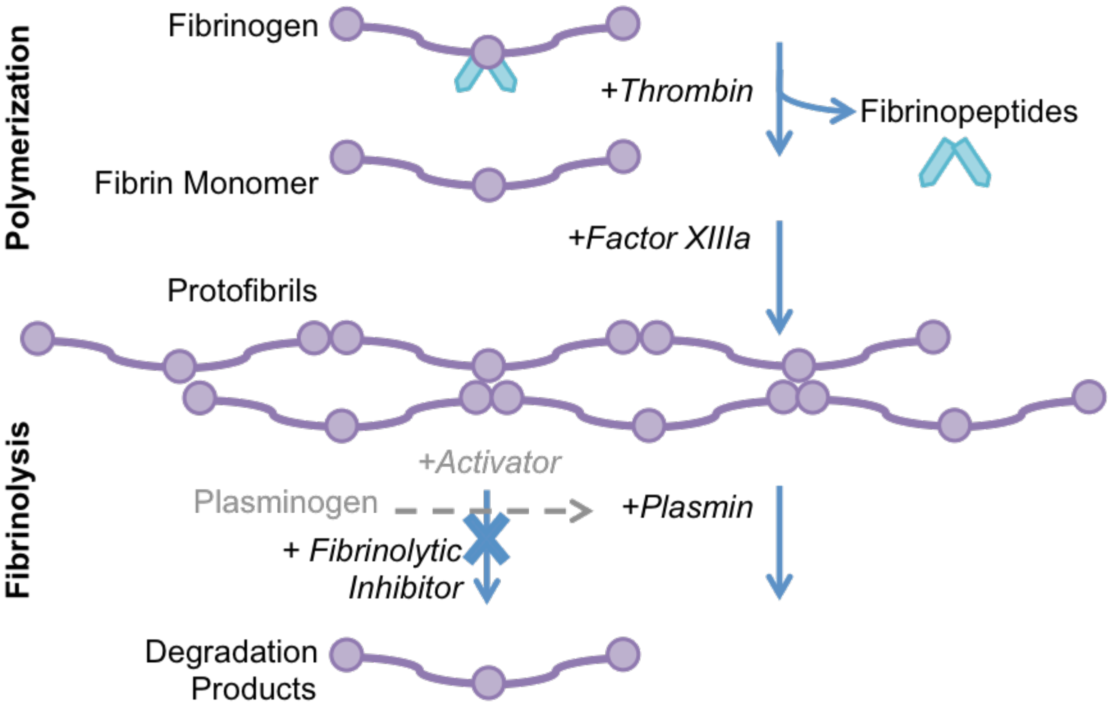

Figure 2.3: Polymerization and degradation of fibrin. Fibrinogen is cleaved by thrombin to produce a fibrin monomer, which polymerizes to form protofibrils. Plasmin (which forms when plasminogen is activated) can degrade fibrin unless inhibited by a fibrinolytic inhibitor.

2.3.2 Fibrinolysis and Anti-Fibrinolytic Agents

The process of coagulation and clotting (fibrin polymerization) is actively and equally opposed in a physiological equilibrium by fibrinolysis, a system that removes fibrin residues that could otherwise permanently occlude the vascular system. Despite cross-linking by Factor XIIIa during polymerization, fibrinogen is extremely susceptible to degradation by proteases. Plasminogen is activated as plasmin by an activator such as tissue-type plasminogen activator (tPA); plasmin then cleaves fibrin at specific sites (**Figure 2.3**). Fibrin can act as both a substrate and a cofactor for plasmin; molecules can promote the generation of plasmins that degrade the clot, which can be useful for renewing the blood supply to cells at the clot site (Weisel, 2007; Wolberg, 2007). Natural inhibitors of plasmin and plasminogen activators (tissue activator, urokinase, or streptokinase) are present in the circulatory system to prevent indiscriminate fibrinogen digestion. Plasmin is a protease secreted by many different cells to rapidly degrade fibrin after the affected area is restored to its original structural integrity. The entire process is regulated by positive and negative feedback loops; unchecked fibrinolysis can result in hemorrhage (Kupcsik et al., 2009; Prentice, 1980).

Degradation by plasmin and resulting fibrin instability is a drawback to tissue engineering with fibrin, and a plasmin inhibitor must be incorporated for systems lasting longer than a few hours. ε-Aminocaproic acid (ACA) and aprotinin are anti-fibrinolytic agents that inhibit the degradation of fibrin by serine proteases such as plasmin, thus maintaining structural integrity. ACA binds to the lysine binding sites present on both plasmin and plasminogen, preventing plasmin from being activated and binding to (and subsequently degrading) fibrin by competitive and stoichiometric inhibition. Kupcsik *et al*. studied the use of ACA on chondrogenic differentiation of human mesenchymal stem cells (hMSCs) and its general use in cartilage engineering constructs. They found that it did not significantly affect gene expression patterns or glycosaminoglycan (GAG) production, thereby proving its long-term usefulness in tissue engineered systems (Kupcsik et al., 2009; Valentovic, 2007). Huang *et al*. compared the effects of ACA and aprotinin on rat bone marrow mesenchymal stem cell (BM-MSC) chondrogenesis in fibrin constructs. BM-MSCs are naturally recruited to repair articular cartilage defects as a result of blood flow disruption when a clot forms. The two proteins have different mechanisms of plasmin inhibition, but no significant difference in their effects on DNA content was observed (Huang et al., 2007). However, in comparison to ACA, aprotinin can be expensive to isolate and is a less specific inhibitor of plasmin (Kupcsik et al., 2009).

2.3.3 USE OF FIBRIN IN TISSUE ENGINEERING AND DRUG DELIVERY

Fibrin is an attractive biomaterial because, unlike synthetic hydrogels, it naturally displays two RGD sites that allow it to bind cell integrins, vascular endothelial cadherins, growth factors, and other proteins (fibronectin, hyaluronic acid, and albumin) (Bach et al., 1998; Janmey et al., 2009; Weisel, 2005). Its high water content and biodegradability also greatly support cell processes, and it displays a similar structure *in vitro* and *in vivo* (Kidd et al., 2012). The abundance and ease of purification of fibrinogen from a patient's own bloodstream also make it an appealing biomaterial for *in vivo* and clinical studies by eliminating the possibility of an immune response (Lei et al., 2009). Additionally, gelation time of fibrin can be meticulously controlled by altering the concentrations of fibrinogen and especially thrombin (Janmey et al., 2009). Pore size, degree of branching, and fiber thickness can be dictated by the polymerization conditions (including parameters such as pH, and concentration of plasma proteins), and cell migration and differentiation within the matrix can be made more efficient by controlling its mechanical and biochemical properties (Weisel, 2007). Because of its wide range of capabilities, fibrin has been used in almost every tissue engineering application over the past decade and a half, from wound repair to drug delivery, cell differentiation, and therapeutic scaffolds for cardiovascular repair, regenerative medicine, and angiogenesis.

Kidd *et al.* used fibrin hydrogels with hydroxyapatite (HA) particles as carriers for lentiviral gene delivery, easily tailoring the release profile by altering the interaction of the scaffold and the drug or growth factor (Kidd et al., 2012). Alternatively, fibrin can be injected *in vivo* to form a gel and be naturally degraded as a biopolymer. Lei *et al.* used fibrin as a gene delivery system by embedding DNA in the gel prior to polymerization. The gel system permitted spatial distribution of transfection while minimizing toxicity. Fibrinolytic inhibitors actually slowed the degradation process and resulted in decreased transfection efficiency, demonstrating the application-specific need for fibrin scaffold degradation (Lei et al., 2009). Fibrin gels have also been utilized as a scaffold to deliver MSCs to a wound site, promoting bone formation and healing in degradable delivery mechanism. The use and delivery of MSCs is promising for therapeutic applications, as the stem cells have the capacity to differentiate into chondrocytes, adipocytes, myoblasts, and osteoblasts (Bensaïd et al., 2003).

Fibrinogen's human origin renders it an attractive biomaterial and a potentially autologous transplant device. The benefits of fibrin in clinical tissue engineering have recently been demonstrated by the development of a bioengineered ocular surface, an "injectable" liver to transferred immobilized hepatocytes, millimeter-scale vascular grafts seeded with arterial-derived cells, and engineered aortic heart valves made from dermal fibroblasts within molded gels (Bruns et al., 2005; Han et al., 2002; Koch et al., 2010; Robinson et al., 2008).

2.3.4 USE OF FIBRIN IN MUSCLE ENGINEERING AND REGENERATION

The interactions of human myocytes and fibrin matrix in a physiologically relevant 3D culture model were characterized extensively by Chiron *et al.* in 2012. The morphology of embedded myoblasts changed from a round shape upon polymerization to an elongated formation oriented along the gel axis on the first day, which was attributed to the cells re-orienting themselves in relation to the tension provided by the silicone structures. $\alpha 5$ integrin and vinculin were more highly expressed in 3D than 2D cultures, and actin stress fibers had a prevalent orientation along the direction of the gel alignment and cell orientation. Whereas fused myotubes can be branched and randomly aligned in 2D, the cells observed in 3D culture were aligned along the gel axis. The elastic modulus of the gels increased with cell differentiation over time, demonstrating the implications of microenvironment and substrate elasticity on cell organization and fate. The increase in stiffness (which was measured to be similar to the value of native skeletal tissue) with differentiation also implied the important role of cell contractility (Chiron et al., 2012). Previously, Engler *et al.* had shown that the formation of sarcomeres in cultured myocytes was dependent on the stiffness of the substrate being nearly equal to that of physiological muscle (Engler et al., 2004).

Many groups have successfully employed fibrin for muscle tissue engineering and regeneration. Beier *et al*. mixed fibrin gel with myoblasts to create a novel injectable cell-matrix solution to fill a muscle fiber defect (Beier et al., 2006). A bioengineered cardiac heart muscle developed by Hecker and colleagues used primary cardiomyocytes and a fibrin support matrix within a micro-perfusion system that regulated pH, temperature, and rate of media flow in a physiological environment to encourage tissue viability (Hecker et al., 2008). More recently, Gerard *et al*. examined the use of fibrin gels to encapsulate and transplant myoblasts as a regenerative therapy for dystrophin restoration in Duchenne Muscular Dystrophy. Gel degradability and cell proliferation were measured for different fibrinogen concentrations, with a lower concentration (3 mg/ml) proving the most effective for increasing cell survival, metabolic activity, and dystrophin expression (Gerard et al., 2012).

2.4 SKELETAL MUSCLE ENGINEERING

2.4.1 SKELETAL MUSCLE PHYSIOLOGY AND DEVELOPMENT

Skeletal muscle is the only type of voluntary muscle in the human body. It connects to the skeleton via tendons and supports movement, locomotion, respiration, and other activities (Watras, 2008). The formation of skeletal muscle in embryogenesis begins with progenitor cells in the vertebrate limb. Extensive proliferation of progenitor cells is followed by the expression of deterministic myogenic factors and finally differentiation into skeletal muscle (**Figure 2.4A**) (Buckingham et al., 2003). In adult tissue, satellite cells are present in a quiescent state under the basal lamina along the myofibers (Li et al., 2011). Injury to adult muscle or other stimulation results in activation of these progenitor cells and subsequent division and differentiation into new myofibers (Gerard et al., 2012).

During myogenesis, the fusion of myoblast precursor cells produces multi-nucleated myotubes with one cytoplasm. Commitment to a myogenic lineage involves withdrawal from the cell cycle and the expression of genes that are specific to muscle (Duan et al., 2010). Muscle growth begins with primary fibers, which eventually become slow-twitch fibers; when the primary fibers become innervated, secondary fibers (fast-twitch) form around them (Ontell & Kozeka, 1984). Three layers of connective tissue (endomysium surrounding individual fibers; perimysium, encompassing the fascicles; and epimysium surrounding the entire muscle) surround skeletal muscle *in vivo* as a barrier from physical stress and damage (Khodabukus & Baar, 2009; Watras, 2008).

Adult skeletal muscle is longitudinally aligned and multi-nucleated in a modular hierarchy, beginning with single fibrils that group together to form fibers and fascicles (**Figure 2.4B**) (Li et al., 2011; Watras, 2008). Over this wide range of length scales, however, the relationship between structure and function is maintained. This range also accounts for the span of observed forces, frequencies, and dimensions of skeletal muscle. Contraction can reach a frequency upwards of 100 Hz, with forces reaching over a kilo-Newton, and the length of skeletal muscle extending over 1 meter in some organisms (Feinberg et al., 2007).

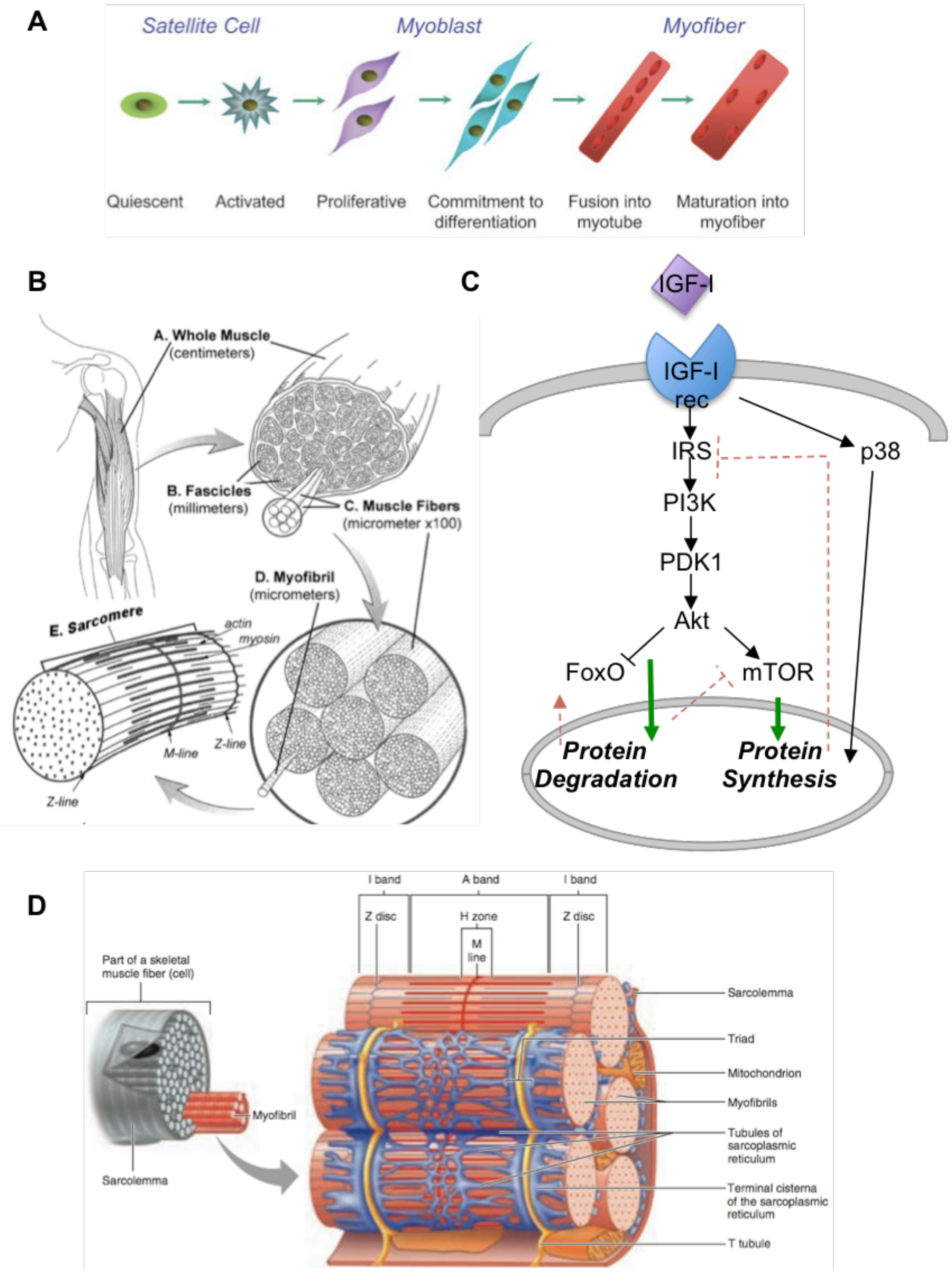

Figure 2.4: Skeletal Muscle. (A) Myogenesis: activation, proliferation, and differentiation (Zammit et al., 2006) (B) Skeletal muscle hierarchy and dimensions (Lieber, 2002) (C) Intracellular signaling cascade of IGF-I resulting in protein synthesis or degradation (D) Organization within a myofibril (Marieb, 2006)

The organization of actin and myosin within skeletal muscle sarcomeres produces a striated structure in the myofibrils (**Figure 2.4D**). The sarcoplasmic reticulum surrounds individual myofibers and controls the concentration of calcium ions (a key regulator of contraction and force production) within the cell. An action potential traveling along the sarcolemma reaches a T-tubule (an invagination of the sarcolemma), resulting in a release of Ca^{2+} ions from the sarcoplasmic reticulum. After the intracellular concentration of Ca^{2+} increases, the ion binds to troponin C, resulting in a shift of the tropomyosin molecule away from the myosin binding site on actin. Actin-myosin binding initiates sarcomere shortening and contraction of the muscle (Watras, 2008).

The basement membrane of skeletal muscle is referred to as the basal lamina and its formation is initiated by fibroblasts. The role of the basal lamina in providing the necessary elasticity and strength for muscle is of critical importance. It also provides key binding sites for the sequestration of myogenic growth factors for muscle development and helps to maintain neuromuscular junctions (NMJs). Collagen IV, laminin-2, and proteoglycans are present in abundance in skeletal basal lamina. Fibroblasts also play a role in myofiber maturation and support.

2.4.2 Need and Overview

The engineering of functional skeletal muscle is imperative for regeneration and replacement of pathologically damaged or injured native tissue. These defects and myopathies are somewhat ‘doomed’ by the limited self-regeneration of skeletal muscle and therapeutic strategies that cannot overcome limited survival of transplanted cells and donor site morbidity.

Extracellular matrix proteins such as collagen I and fibrin are natural hydrogels that allow for muscle cell proliferation and spreading, alignment of cells in a common direction, and tissue contraction on a macroscopic scale. As such, they have been used in abundance as supportive proteins for skeletal muscle engineering, and have been more successful than delivering precursor cells to an injury site. An organized ECM surrounds native skeletal tissue in the basal lamina. As is the case with many diverse cell types, the ECM also contributes to the maintenance of cellular processes and communication in normal growth and development of skeletal cells (Bian & Bursac, 2008; Hinds et al., 2011). However, the volume fraction of extracellular material is small compared to that of the fibers in muscle tissue, and an engineered muscle construct with excess ECM material could hinder myotube formation and constrain specific force (Huang et al., 2005).

2.4.3 ENGINEERED MUSCLE CONSTRUCTS

A novel technique to rapidly form engineered skeletal muscle constructs with ECM proteins was developed by Huang *et al.* in 2005. The researchers used fibrin gel to create three-dimensional tubules of primary myoblasts and matrix protein that contracted around a pair of sutures 12 mm apart on a PDMS-coated dish. The decision to use fibrin protein was multifold: it allowed for cell migration and proliferation, was degraded after a few weeks as cells produced their own matrix proteins, and could bind to some myogenic growth factors. A force transducer was attached to one end of the muscle cylinder and electrical stimulation was applied. The tissue constructs contracted maximally with a tetanic force greater than 800 μN after three weeks in culture, and addition of 25 ng IGF before seeding resulted in a significantly increased force output. The force-frequency and length-time relationships were reported on the same scale as those of native skeletal tissue (Huang et al., 2005).

Bian, Bursac, and colleagues first developed an array of staggered micro-molded hexagonal PDMS posts around which skeletal tissue and hydrogel networks could form in a spatially controlled manner. The placement of the posts allowed for "microfabricated tissue pores" that guided the alignment and organization of dense myofibers and endorsed diffusion of nutrients and oxygen to the cells. The ability to change the position and architecture of the posts allowed for various degrees of muscle tissue arrangement, morphology, and complexity (Bian & Bursac, 2009; Bian et al., 2009). This technology was improved when Bian and Bursac studied the effect of pore length and geometry on the morphology, alignment, myogenesis, and contraction of engineered muscle. Pore elongation increased cell alignment and total contractile force without compromising individual myofiber force capability. The resulting widening of the pores (i.e., narrowing of tissue bundles) also increased the porosity of the tissue, demonstrating global changes on functional output from local changes in tissue architecture (Bian et al., 2012).

A study by Khodabukus and Baar examined the use of fibrin as a matrix system for engineered skeletal muscle tissue in place of collagen, which they hypothesized would allow for more accurate functional testing, as fibrin has mechanical properties and stiffness similar to native muscle tissue. Because two-dimensional structures cannot provide accurate measurements of muscle cell force, especially since stiff culture surfaces limit myogenesis in favor of osteogenesis, three-dimensional constructs with fibrin matrix were used to engineer muscle using C2C12 cells and NIH/3T3 fibroblasts. Electrical force stimulation was applied via electrodes on either side of the muscle constructs. The constructs with aprotinin formed more quickly and produced a higher specific force over time. The researchers found that maximal force production was significantly affected by C2C12 clonal variations as well as variations in the serum batch and the serum content in the media. The addition of fibroblasts eliminated the force deficit (decrease in twitch force after stimulation), but also decreased the specific force of the constructs. Output forces ranged between 100-200 μN and were not significantly altered after repeated testing for weeks. They also proved that high serum media resulted in faster differentiation and increased force (Khodabukus & Baar, 2009).

Hinds and colleagues recently studied the effect of ECM composition and density on the formation and functional contractile force output of engineered skeletal muscle constructs similar to those used by Huang *et al*. Fibrin, collagen I, and Matrigel of varying concentrations were combined with primary skeletal muscle myoblasts in a gel solution and allowed to form muscle bundles in silicone molds. Spontaneous contractions were evident after about a week of culture, and continued to be observed for the duration of the study at a frequency of less than 3Hz. The bundles were removed after two weeks and analyzed in terms of active and passive tension. The choice of ECM protein did not affect cell organization or spontaneous contractions in the muscle bundles, but different matrix proteins demonstrated various degrees of compaction, with collagen based fibers exhibiting the highest passive tension and stiffness, as well as compaction (in contrast to the findings of Bian and Bursac), but greatest degree of rupture. Higher concentrations of both fibrin and Matrigel reduced bundle compaction and average myotube diameter while increasing time to tetanus. In total, the researchers found that the bundles made of fibrin demonstrated a higher degree of mechanical integrity and generated contractile forces that were measured to be three times greater than those made of collagen I. The most optimal conditions (producing the highest force of contraction and largest myotube diameters) came from the gels made of 4 mg/mL fibrinogen and 40% Matrigel, demonstrating the impact of matrix composition on functional output (Hinds et al., 2011).

Li *et al*. created muscle from primary mouse myoblasts (PMMs) and mouse embryonic fibroblasts (MEFs) from pregnant mice in various ratios to study the role of fibroblasts in skeletal muscle self-assembly. The cells were allowed to self-assemble into muscle constructs on 3D laminin and fibrin gels. Alignment in 3D resulted from the tensile forces from the spontaneous contraction of the muscle strip, as well as the tension generated by the fibrin gel. After 10 days in differentiation media, a physiological fascicle-like structure had formed with aligned cells. Staining confirmed that the structure contained ~500 nuclei through the diameter and that the myofibers were mature (multinucleated with sarcomeric striations). The muscle constructs formed in 3D were significantly longer than those formed in the 2D culture. When the PMMs were co-cultured with MEFs in an optimal 1:1 ratio, the viability, size, and number of myotubes increased significantly, most likely due to the role that fibroblasts play in the secretion of growth factors during myogenesis. It was also hypothesized that the MEFs played a role in degradation of the fibrin scaffold and decreasing the stiffness of the construct, thereby producing a sufficient force of contraction to roll up the cell sheet (Li et al., 2011).

Nagamine and colleagues devised a method to micropattern C2C12 myotubes in a flexible fibrin-PDMS sheet for a practical cell-based bioassay technology. Following differentiation in culture on a line-patterned polymer, cells were transferred onto the sheets after the fibrin solution was added over the cells. Another layer of fibrin was added onto the other side of the sheet to encapsulate the cell patterns within the gel, and concentrated electrical stimulation was applied using a conducting polymer-coated microelectrode arrays. The presence of the polymer allowed for long-term stimulation in a minimally invasive and harmful manner. Each microelectrode could be controlled to induce independent contraction of the cell pattern lines. The system was used as a functional metabolic bioassay to monitor translocation of a glucose transporter within the myotubes upon contraction (Nagamine et al., 2011).

A "skeletal muscle on a chip" was created by Sakar *et al*. using a C2C12 myoblast-Matrigel-collagen I matrix suspension that was allowed to compact longitudinally around cantilevers in a PDMS microwell. The myoblasts were transfected with a plasmid to express channelrhodopsin-2 (ChR2), an optogenetic ion channel that causes contraction upon exposure to blue light (see **Section 5.1**). The ability to illuminate (stimulate) individual myofibers permitted localized and selective contraction and movement of the pillars with multiple degrees of freedom. The cantilevers provided simultaneous reporting of the force generation (10.8 ± 0.18 μN static tension with an active force of 1.41 ± 0.25 μN generated from contraction) while acting as functional artificial tendons to anchor the muscle tissues. The researchers argued that the factors that define skeletal from cardiac muscle (namely, length and structure) allow for greater force production and regulation (Sakar et al., 2012).

2.4.4 INSULIN-LIKE GROWTH FACTOR-I AND MYOGENESIS

Insulin-like growth factors (IGFs, so-called because of their evolutionary conserved structures that are similar to insulin) are part of a family of proteins that play a role in skeletal tissue growth in many vertebrate species through autocrine and paracrine mechanisms. Binding of the IGF ligand to a cell membrane IGF-receptor triggers an intracellular signaling cascade that terminates with regulation of genes and transcription factors in the nucleus. Specifically, insulin-like growth factor I (IGF-I) encourages myoblast proliferation and differentiation as well as myofiber hypertrophy (Duan et al., 2010; Shansky et al., 2006). However, while the effects cascade from the same IGF receptor, these processes are independently regulated on different temporal scales. Proliferation results from myogenic inhibition and is exclusive of myogenic differentiation events (Florini et al., 1991).

The IGF-I pathway is highly conserved and affects skeletal muscle growth through protein synthesis and degradation (**Figure 2.4C**). After IGF-I binds to a cell-surface receptor, intracellular kinase is activated, resulting in subsequent and sequential phosphorylation of insulin receptor substrate (IRS), phosphatidylinositol-3-kinase (PI3K), phosphoinositide-3,4,5-triphosphate (PIP3), and finally Akt. The Akt kinase is a key player in the cascade and regulates mammalian protein synthesis through targeting of rapamycin (mTOR) kinase, as well as protein degradation through the FoxO family of transcription factors, which are responsible for expression of ligases that ubiquitinate myosin muscle proteins (Manning & Cantley, 2007). Additionally, IGF-I or –II receptor binding can also activate the p38 MAPK pathway to promote differentiation (Duan et al., 2010). Many feedback loops are used to regulate these pathways within the cell.

Salmon and Daughaday were the first to validate that growth hormones could release growth factors such as IGF into the bloodstream from the liver, while Hill and colleagues proved that cultured myoblasts could also release IGFs. Since then, many knockout studies have validated the important role of IGF in skeletal muscle development by examining each component of the IGF pathway (Florini et al., 1996; Hill et al., 1984; Salmon & Daughaday, 1957).

In contrast, many groups have studied the effect of IGF addition on growth and hypertrophy. Over-expression of IGF-I has been recognized to increase muscle fiber size and strength while decelerating muscle decline in differentiated myofibers (Barton et al., 2002; Barton-Davis et al., 1998). Vandenburgh and colleagues demonstrated the use of IGF-I to quickly increase the diameter (hypertrophy) of skeletal muscle myofibers embedded in collagen. After 5 days in culture they observed a 79% increase in myofiber diameter and 87% more nuclei, a direct result of the role of IGF-I in stimulating protein synthesis and inhibiting protein degradation (Vandenburgh et al., 1991). Shansky *et al.* engineered constructs of C2C12 skeletal muscle cells that secreted IGF-I and monitored the effect on co-cultured avian skeletal muscle in a perfused bio-chamber. After 11 days, levels of IGF-I in the avian muscle chamber increased linearly, and cells in that chamber displayed significantly larger myofibers (and in greater quantity) than the non-secreting C2C12 control. This proved that secretion of IGF-I from transduced myoblasts was adequate to produce a direct paracrine effect on non-transduced myoblasts (Shansky et al., 2006). Finally, differentiation of myoblasts into myotubes (highly regulated by MyoD, Myf5, myogenin, and various transcription factors) has been shown to accelerate with the addition or over-expression of IGFs (Buckingham et al., 2003; Ren et al., 2008; Stewart et al., 1996).

3. METHODOLOGY

3.1 DESIGN AND FABRICATION

3.1.1 MATERIALS

The pre-polymer solution for the bio-bot consisted of 20% (v/v) poly(ethylene glycol) diacrylate of M_W 700 g/mol (PEGDA M_W 700, Sigma-Aldrich) dissolved in phosphate buffered saline (PBS, Lonza), with 0.5% (v/v) 1-propanone, 2-hydroxy-1-[4-(2-hydroxyethoxy)phenyl]2-methyl- photoinitiator (Irgacure 2959, BASF) mixed from a 50% (v/v) stock solution in dimethyl sulfoxide (DMSO, Fisher Scientific) (**Figure 3.1A**). The pre-polymer solution for the polymerized holder was made from 20% (w/v) poly(ethylene glycol) dimethacrylate of M_W 1000 g/mol (PEGDMA M_W 1000, Polysciences, Inc.), dissolved in PBS, and mixed with 0.5% (v/v) Irgacure 2959 diluted from a 50% (v/v) stock solution in DMSO.

3.1.2 PREPARATION AND FABRICATION

A Stereolithography Apparatus (SLA) was used to selectively polymerize the material by tracing a pattern on the surface of the pre-polymer liquid with a 325nm HeCd gas laser. After polymerizing the first layer, the stage moves down a distance that is equal to the height of the first layer, the surface is re-coated with another layer of pre-polymer solution, the laser beam is re-focused, and the second layer is polymerized. The additive process continues in this “bottom-up” fabrication method until the entire part is built.

A commercial SLA System (250/50, 3D Systems, **Table 3.1**) was modified for polymerization as previous described (Chan et al., 2010). Briefly, the parts were designed in AutoCAD (2013, Autodesk) and then exported to 3D Lightyear software (1.4, 3D Systems), which was used to slice the part into 2D layers for the SLA. To build the bio-bots, a 35mm petri dish (BD Falcon) was treated with an O_2 plasma treatment system to render the surface hydrophilic. An 18x18 mm square No. 1 micro cover glass (VWR) was secured to the center of the dish using double-sided tape. The dish was placed in the center of the stage and an initial volume of 1200 µl of PEGDA M_W 700 pre-polymer solution was added with a pipette for polymerization of the bio-bot beam. D_P was altered to change the polymerization energy of the beam. 250 μl of pre-polymer solution was added manually for each subsequent polymerized layer, which became the bio-bot pillars (**Figure 3.1B**). The polymerization energy was not altered for the pillars.

To build the holder for the bio-bot, a 35 mm dish was similarly treated with an O_2 plasma treatment system. The cover glass slides were methacrylated by treatment with 0.2% (v/v) 3-(trimethoxysilyl)propyl methacrylate (3-TPM, Sigma-Aldrich) in 200 proof ethanol (100% EtOH, Decon Labs, Inc.) on a shaker for 5 minutes. The 3-TPM solution was removed and the slides were washed in 100% EtOH on a shaker. After 3 minutes, the slides were removed and allowed to dry face-up on a hot plate at 110ºC for 10 minutes. Finally, each slide was taped face-up in a 35 mm dish and polymerization occurred as described above.

Laser Type	Gas (HeCd)
Wavelength	325 nm
Max Power	40 mW
XY Resolution	250 μm
Z Resolution	50 μm

Table 3.1: SLA 250/50 system specifications

3.1.3 POST-PROCESSING OF FABRICATED PARTS

Immediately following fabrication, each bio-bot or holder structure was placed in a dish and immersed in PBS on a shaker for 5-10 minutes to be rinsed of excess pre-polymer solution. The fabricated structures were sterilized in 70% ethanol for 1 hour and transferred to a dish containing PBS to re-swell for at least 1 hour. Structures were stored in PBS at 4ºC until use (**Figure 3.1C**). Before cell seeding, each fabricated bio-bot structure was positioned upside down in a holder, which was placed in a 35 mm cell culture dish (Corning, Inc.). Excess liquid was aspirated using a glass Pasteur pipette.

3.2 CELL CULTURE

3.2.1 GROWTH CONDITIONS

C2C12 murine myoblasts were transfected with pAAV-Cag-Chr2-GFP-2A-Puro plasmid to express ChR2 as described in (Sakar et al., 2012). Cells were a gift from Prof. Harry Asada at MIT.

The ChR2 C2C12 cells were maintained in growth medium (GM) in a cell culture incubator at 37ºC and 5% CO_2. GM consisted of Dulbecco's Modification of Eagle Medium with L-glutamine and sodium pyruvate (DMEM 1X, Corning Cellgro), supplemented with 10% fetal bovine serum (FBS, Lonza), 1% penicillin-streptomycin and 1% L-glutamine (Cellgro Mediatech, Inc.).

3.2.2 DIFFERENTIATION

Differentiation medium (DM) consisted of DMEM with 2% or 10% horse serum (HS, Lonza) and supplemented with 1% penicillin-streptomycin and 1% L-glutamine. Human insulin-like growth factor-I (IGF-I, Sigma-Aldrich) and anti-fibrinolytic 6-aminocaproic acid (ACA, Sigma-Aldrich) were added as described in **Table 3.2**.

Name	*Serum*	*IGF-I (ng/ml)*	*ACA (mg/ml)*
GM	10% FBS	0	0
DM(2%HS)	2% HS	0	0
DM(2%HS+IGF)	2% HS	50	0
DM(10%HS)	10% HS	0	0
DM(10%HS+IGF)	10% HS	50	0
DM(10%HS+ACA)	10% HS	0	1
DM(10%HS+ACA+IGF)	10% HS	50	1

Table 3.2: Differentiation medium components

3.3 FORMATION OF CELL-MATRIX MUSCLE STRIP

3.3.1 CELL SEEDING AND MATRIX COMPONENTS

An ice-cold cell-matrix solution of Matrigel basement membrane matrix (30% of total cell-matrix volume, BD Biosciences), fibrinogen (4 mg/ml, Sigma-Aldrich), thrombin from bovine plasma (0.5 U/mg fibrinogen, Sigma-Aldrich), and ChR2 C2C12s suspended in cold GM at a concentration of $5x10^6$ cells/ml were added to each holder in a total volume of 90 μl (hour 0) (**Figure 3.1D**). At hour 1, 4 ml of GM was added to each 35 mm dish. At hour 24, the bio-bots were released from the holders and the appropriate DM was added to induce differentiation of the myoblasts into myotubes (**Figure 3.1E**). The media was changed every 24 hours thereafter and the bio-bots were transferred to new 35 mm tissue culture dishes as necessary. The bio-bots were maintained in a cell culture incubator at 37ºC and 5% CO_2.

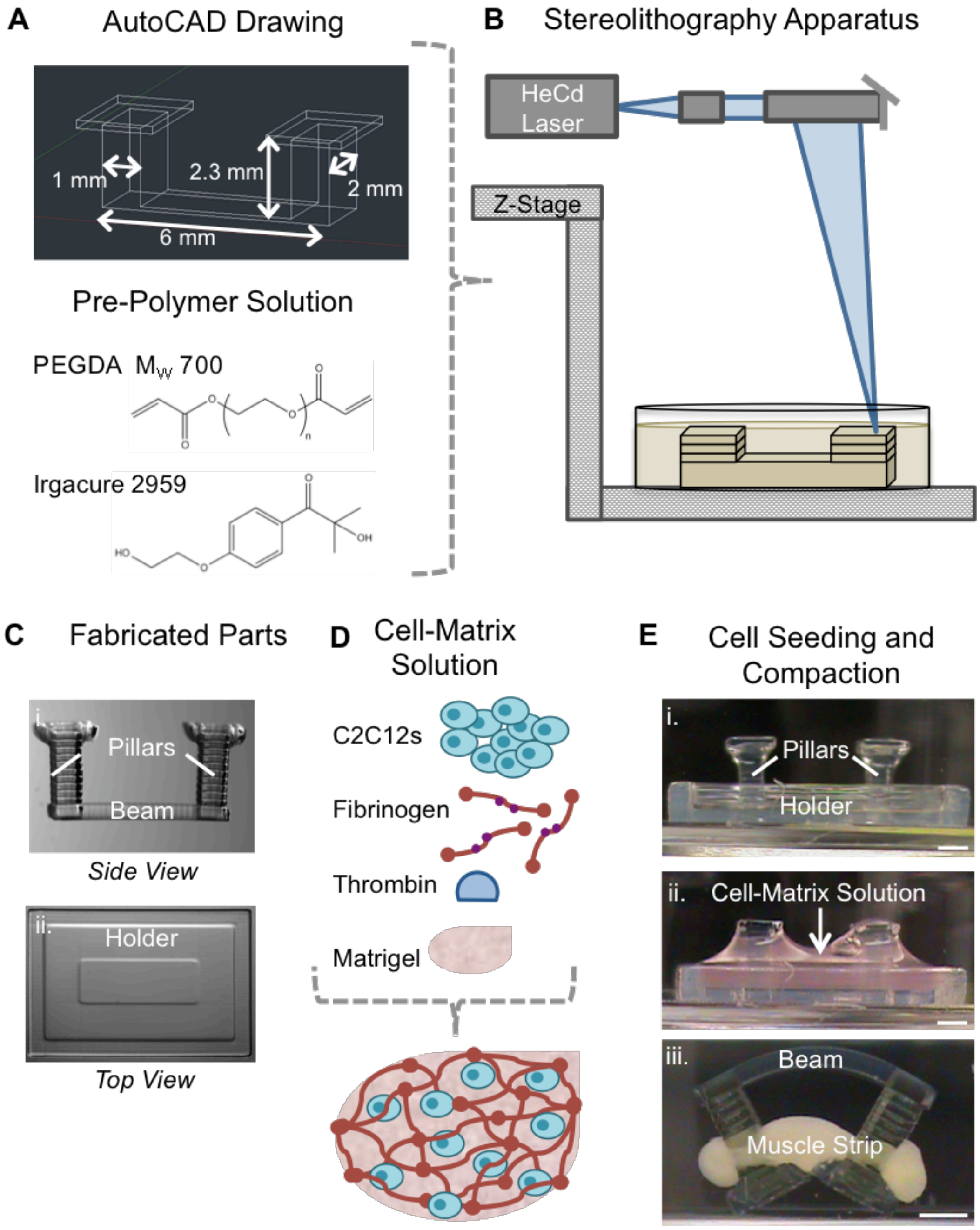

Figure 3.1: Fabrication And Cell Seeding Process. (A) AutoCAD software is used to design the bio-bot with the desired dimensions. A pre-polymer solution consists of poly(ethylene) glycol diacrylate (PEGDA) M_W 700 and a photoinitiator, Irgacure 2959. (B) A modified commercial stereolithography apparatus (SLA) is used to polymerize the parts in an additive process with a 325 nm HeCd gas laser. (C) The polymerized parts: i, bio-bot; ii, holder. (D) The cell-matrix solution consists of C2C12 skeletal muscle myoblasts, fibrinogen, thrombin, and Matrigel. (E) Side-view images of the addition of cell-matrix solution into the holder containing the bio-bot (i-ii). The cells and matrix contract around the pillars to form a muscle strip and the device is released from the holder (iii). Scale bar, 1 mm.

3.3.2 COMPACTION AREA

To measure the cross-sectional compaction area, the holders containing the bio-bots seeded with the cell-matrix suspension were imaged at 0.8X zoom using a stereomicroscope (MZ FL III, Leica Microsystems) with a digital microscope camera (Flex, SPOT Imaging Solutions) at hours 1, 6, 9, 12, and 24. The Measure tool in ImageJ software (National Institutes of Health, NIH) was used to calculate the cross-sectional area by quantifying the visible compacted area of the cell-matrix solution and subtracting the cross-sectional area of the pillars.

3.4 MATERIAL CHARACTERIZATION

3.4.1 WORKING CURVE

Cylinders with a radius of 1 cm and a height of 100 μm were fabricated from PEGDA M_W 700 with 0.2 μm Nile Red fluorescent microbeads (Spherotech) encapsulated in a 1:500 ratio of beads to polymer. E_{max} was varied from 71 to 512 mJ/cm^2 by maintaining a constant E_C value and changing the input D_P value. The thicknesses of the fabricated parts (C_D) were measured using an inverted fluorescent microscope (IX81, Olympus) with a TRITC excitation filter. The beads encapsulated in the bottom-most plane of the cylinder were brought into focus and this location was set as zero. The focus was then set on the top-most plane of encapsulated beads in the cylinder and this change in displacement was recorded as the height of the cylinder. Four parts were fabricated for each energy dose and an average height was taken from four points per part. The average thickness was plotted against the applied energy dose and a logarithmic trendline was fit to the data to create a Working Curve.

3.4.2 MECHANICAL TESTING AND DETERMINATION OF ELASTIC MODULUS

To characterize the mechanical properties of the material (PEGDA M_W 700), dogbone-shaped test specimens were fabricated with the same thickness as that of the bio-bot beam and with energy doses ranging from 95 to 513 mJ/cm^2. Each specimen was fixed in a hydrated sample chamber using custom-fabricated structures and an ElectroForce® BioDynamic® test instrument (5100, Bose) with a 1000 g load cell was used to apply tension at each end. A video extensometer was used to track the displacement of a fixed point on the sample until fracture. The cross-sectional area of the sample was measured three times using calipers and averaged. The stress was then computed using the applied tensile load F divided by the cross-sectional area A. The elastic modulus E was determined from the linear portion of the stress-strain curve for each material, according to Hooke's Law, assuming a slow strain rate:

$$\sigma = \frac{F}{A} = \varepsilon \cdot E$$

The elastic modulus was plotted as a function of the applied energy dose and a logarithmic trendline was fit to the results.

3.5 BENDING AND PASSIVE TENSION

3.5.1 PASSIVE TENSION

Devices were fabricated with a range of energy doses from 95 to 513 mJ/cm^2 for the bio-bot beam. The stiffness of the pillars was kept constant. Cell-matrix solution was added as described above. Side-view images of the bio-bots were taken every 24 hours after seeding using a stereo-microscope at 0.8X zoom with a digital microscope camera.

The passive tension in the muscle strip (i.e., tension at rest) was determined using an Euler-Bernoulli linear beam theory. The differential equation given below relates the deflection of a curved beam to an applied moment:

$$\frac{-Pl}{EI} = \frac{d\theta}{ds} = \frac{y''}{\sqrt{1 - y'^2}}$$

where P is the tension in the muscle strip, l is the moment arm from the muscle strip to the beam, E is the elastic modulus of the beam, I is the moment of inertia of the beam, and y is the deflection of the beam from the horizontal (**Figure 3.2**). With the assumption that the rotation in the beam (y') approaches zero, the right side of the equation is approximated as y'', the curvature. Equating the applied moment M to the tension P times the moment arm l, the equation becomes:

$$\frac{d^2y}{dx^2} = \frac{M}{EI}$$

For a rectangular cross-section, the moment of inertia is determined using the measured dimensions (width, b, and height, h) of the beam:

$$I = \frac{bh^3}{12}$$

Boundary condition (BCs) were applied by assuming zero deflection at the ends of the beam ($L = 0$) and maximum deflection at the center $\left(\frac{L}{2}\right)$. Then, the second-order differential equation was solved for y:

$$y = \frac{My^2}{2EI} - \frac{MLy}{2EI}$$

The maximum deflection (δ_{max}, measured using ImageJ) at the center of the beam was calculated using the previous equation:

$$\delta_{max} = \left| y\left(\frac{L}{2}\right) \right| = \frac{ML^2}{8EI}$$

This equation was rearranged to solve for the moment, M. Again, this quantity is also a product of the passive tension force P in the muscle strip and the moment arm l:

$$M = \frac{8EI\delta_{max}}{L^2} = Pl$$

The dimensions of the beam and moment arm were found using the Measure Tool in ImageJ. Three measurements were taken for each dimension of each device and averaged.

Solving the equation for P yields a measure of the passive tension in the muscle strip as a function of material and geometric properties as well as the maximum deflection of the beam:

$$P = \frac{8EI\delta_{max}}{l\,L^2}$$

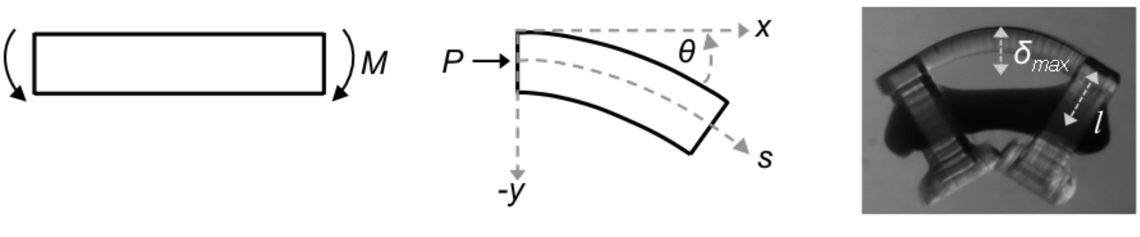

Figure 3.2: Schematic Showing Beam In Compression With Applied Moment. δ_{max} is the maximum deflection of the beam and $\boldsymbol{l}$ is the moment arm from the muscle strip to the beam.

3.5.2 ANSYS SIMULATION AND MODELING

To model the bio-bot, the design was reconstructed using SolidWorks software. The assembly was then imported into ANSYS for finite element analysis. The appropriate material properties and calculated passive tension were assigned and a force was applied to the base at a distance specified by the moment arm (measured in ImageJ). The resultant solution of total deformation was examined to find the maximum deflection of the beam, and this result was compared to the original measurement to determine the error of the simulation.

3.6 IMMUNOFLUORESCENCE

3.6.1 IGF-ANALYSIS IN CULTURE

An *in vitro* study was performed to quantify the effects of IGF-I on ChR2 C2C12 myoblasts. Cells were seeded at a density of 1×10^5 myoblasts per well in a 12-well plate with GM. When cells achieved 90% confluency (day 0), the media was changed to DM(2%HS) or DM(2%HS + IGF). After days 0, 3, 7, 10, 14, and 17, cells were fixed in 4% formaldehyde (from 36% stock solution, EMD Chemicals) and permeabilized with 0.1% Triton X-100 (Sigma-Aldrich) in PBS (PBST) for 10 minutes. A 1% (w/v) blocking solution of albumin from bovine serum (BSA, Sigma-Aldrich) was added for 35 minutes. The cells were then incubated with anti-sarcomeric alpha actinin primary antibody (α-actinin, 1:200, Abcam) with 1% BSA in PBST for 1 hour. Goat anti-Rabbit IgG H&L TRITC-conjugated secondary antibody (1:200 in 1% BSA in PBST, Abcam) was added for one hour in the dark. DAPI nuclear stain (Invitrogen) at a 1:50000 dilution in sterilized DI water was added for 5 minutes in the dark. All steps were carried out at room temperature. Cells were immediately imaged using an inverted fluorescent microscope. Using ImageJ software, red and blue pseudo-color were added to the images for α-actinin and DAPI, respectively, and the number of multi-nucleated myotubes was quantified by counting the cells for each condition and time point and averaging across samples. Results from Day 0 are not shown, as no myotubes were visible.

3.6.2 STAINING AND CONFOCAL IMAGING OF MUSCLE STRIPS

The bio-bot muscle strip was isolated from the device by cutting the pillars and gently removing the muscle strip with tweezers. The tissue was then fixed in 4% paraformaldehyde (from 16% stock solution, Electron Microscopy Sciences) for 30 minutes, washed in PBS, and then permeabilized with 0.2% Triton X-100 for 5 minutes. Image-iT® FX Signal Enhancer (Invitrogen) was added for 30 minutes. The tissue was then incubated with primary antibodies with Image-iT® FX diluted 1:100 in PBS. MF-20 anti-myosin heavy chain (1:100, Developmental Studies Hybridoma Bank (DSHB)) was added for 2 hours. Alexa Fluor® 488 goat anti-mouse IgG secondary antibody (1:200, Invitrogen) was added, and incubation in Image-iT® FX diluted in PBS was carried out for 2 hours in the dark. DAPI nuclear stain was added for 10 minutes in the dark at a 1:5000 dilution in sterilized DI water. The muscle strips were then fixed to a 35 mm glass-bottom microwell dish (MatTek) with 1% agarose gel and imaged with a confocal microscope (LSM 710, Zeiss). Image stacks were acquired and processed using Zen software (2010, Zeiss) and ImageJ.

3.7 ANALYSIS OF ACTUATION

The spontaneous contraction and locomotion of the bio-bots was measured using a camcorder (Handycam DCR-SR65, Sony) on a custom-built stage or an inverted microscope (IX81, Olympus). Displacement was calculated in ImageJ by manually overlaying subsequent frames and measuring the distance traveled during each time point. Frequency was measured by counting the number of contractions in each time segment.

3.8 STATISTICAL ANALYSIS

Results are presented as mean ± standard deviation (SD). Statistical analyses were performed with OriginPro software and represent one-way ANOVA and Tukey's Test.
* represents a significance level of $p < 0.05$ and ** represents $p < 0.01$.

4. RESULTS AND DISCUSSION

4.1 DESIGN AND FABRICATION

4.1.1 WORKING CURVE

The average energy from the SLA is determined by re-arranging the Working Curve Equation (see **Section 2.2.1**, **Figure 4.1A**):

$$C_D = D_P \cdot \ln\left(\frac{E_{max}}{E_C}\right)$$

$$E_{max} = \mathrm{e}^{(C_D/D_P)} \cdot E_C$$

The user can specify the polymerization energy of the 250/50 SLA by changing the D_P and E_C values. When the thickness of the material is plotted against the exposure on a logarithmic scale, the result is a straight line with a slope equal to D_P (Jacobs, 1992).

Increasing the molecular weight of the pre-polymer (from 20% PEGDA M_W 700 to 20% PEGDMA M_W 1000) increased the slope of the Working Curve. Additionally, increasing the PI concentration of Irgacure I2959 from 0.5% to 1% in the PEDGA M_W 700 pre-polymer solution decreased the slope, i.e. the dependence on changes in polymerization energy (**Figure 4.1B**). Fitted trendlines produced values of $R^2 > 0.979$ for all materials. These findings are consistent with the results presented by Arcaute *et al.*; in characterizing the fabrication of PEG-based constructs, it was shown that an increase in PI concentration resulted in thinner gels (Arcaute et al., 2006).

Characterization of the system with variable parameters such as pre-polymer concentration, molecular weight, and PI concentration provided a reference for future designs. A desired layer thickness could be achieved simply by specifying D_P and E_C.

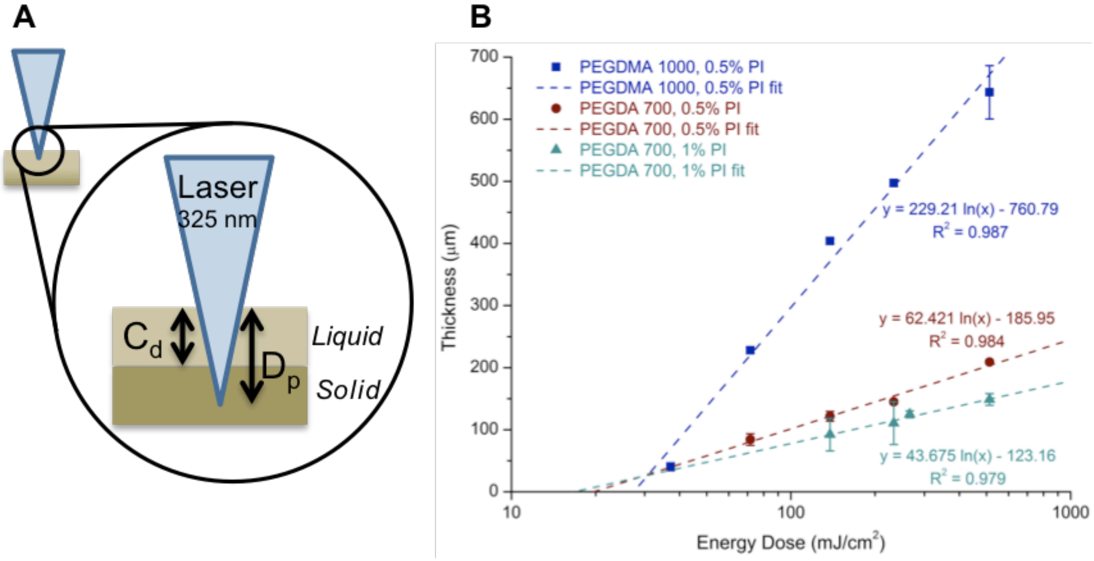

Figure 4.1: Working Curve. (A) The laser penetrates a depth D_P into the material to ensure adherence to the previous layer. The relationship between C_D, D_P, and energy dose is given by the Working Curve equation. (B) The Working Curve was plotted to determine thickness as a function of energy dose for 3 different materials. Increasing the molecular weight and decreasing the PI concentration increased the slope.

4.1.2 MECHANICAL TESTING AND ELASTIC MODULUS

Our group previously observed that changing the polymerization energy from the SLA produced a varying elastic modulus (a measure of stiffness in elastic materials) of a PEGDA hydrogel (Chan et al., 2012). This property was used to "forward engineer" the bio-bot, once again demonstrating the flexibility of design and customization made possible by simply changing input parameters of the SLA.

Because the SLA allows a part to be built in multiple steps, layers can be produced with different materials or properties. We varied the D_P and E_C values to obtain bio-bots with beams of varying stiffness values. All other parameters (material, PI concentration, and pillar stiffness) were kept constant so that only the effect of energy dose on stiffness could be determined. Increasing the energy dose of polymerization logarithmically increased the stiffness (modulus) of the beam material ($R^2 > 0.99$, **Figure 4.2**). These values were used to calculate other quantities of the system, such as passive tension. Characterization of the material properties also provided a basis for future designs that could easily be altered to achieve a specific bending or movement profile.

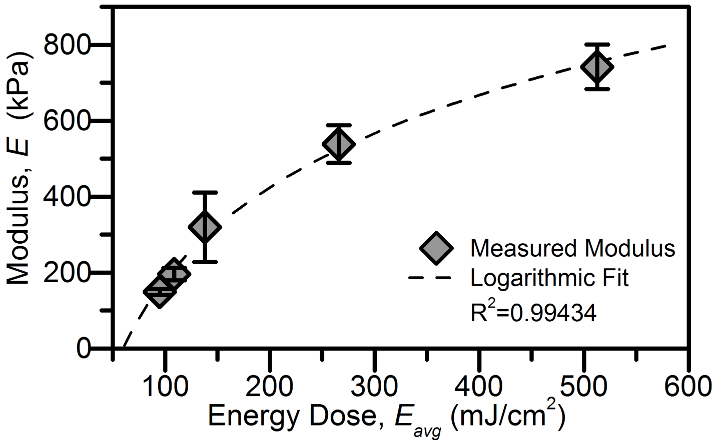

Figure 4.2: Material Properties of the Bio-Bot Beam. The elastic modulus of the beam was calculated as a function of energy dose from a tensile stress-strain curve. Increasing the energy dose of polymerization resulted in a higher modulus. *In collaboration with Mike Poellman*.

4.2 COMPACTION OF MUSCLE STRIP

4.2.1 CROSS-SECTIONAL AREA

An analysis of the top-view images of the cell-matrix solution condensing around the pillars suggested that the cross-sectional area began to stabilize (i.e., the rate of compaction slowed) around hour 24 (**Figure 4.3**). Although compaction continued to occur until hour 48, the bio-bots were released at hour 24, which proved to quicken the remaining compaction around the pillars (data not shown). We hypothesize that the compaction of the cell-matrix solution around the pillars is due to two factors: first, as the cells settle within the matrix, they begin to exert traction forces on the fibrous proteins via integrin attachments; second, polymerization of the fibrin monomers results in a cross-linked polymer gel structure. A greater degree of compaction could indicate a physiological arrangement more similar to native skeletal tissue.

4.2.2 COMPACTION WITH IGF-I

An analysis of the top-view images of the cell-matrix solution compacting around the pillars proved that the addition of IGF-I to DM at hour 24 accelerated the rate of compaction (**Figure 4.4**). The cross-sectional area (shown normalized to the area at hour 24 for each condition) decreased more quickly in the day after IGF-I was added (i.e., at hour 48) compared to the controls without IGF-I. The bio-bots with DM(10%HS + IGF) and DM(10%HS + ACA + IGF) demonstrated a decreased cross-sectional area (26.26% decrease, p = 0.12; and 11.75% decrease, p = 0.16, respectively) compared to the control of DM(10% HS) or DM(10%HS + ACA). Because IGF-I is known to increase the rate of myogenesis (see **Section 2.4.4** and **Figure 4.5**), it is probable that the fused myotubes exerted greater traction forces on the matrix in order to increase compaction.

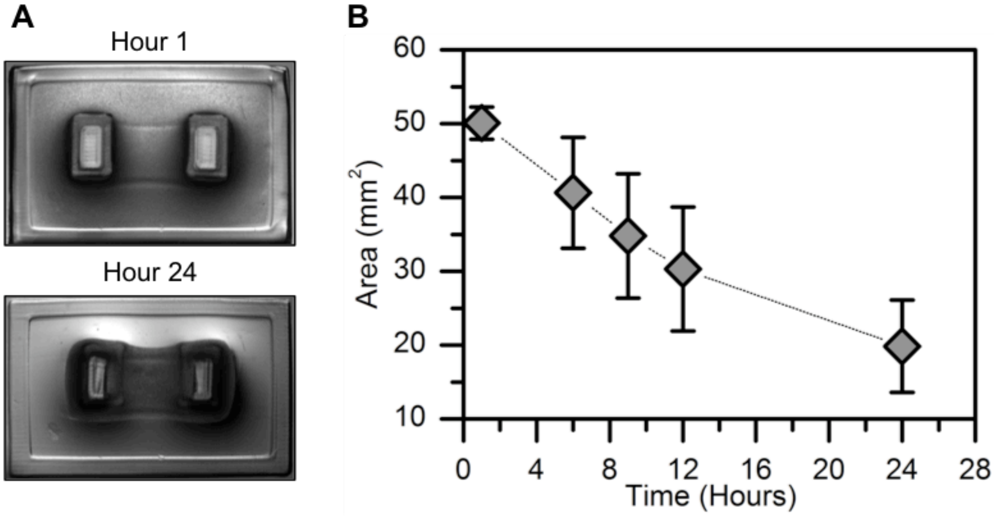

Figure 4.3: Compaction of Cell-Matrix Solution. (A) During the 24 hours after seeding, the cells and fibrin/Matrigel matrix condensed around the pillars to form a solid muscle strip (top view). (B) The cross-sectional area of the muscle strip decreased over the first 24 hours due to compaction; n = 20.

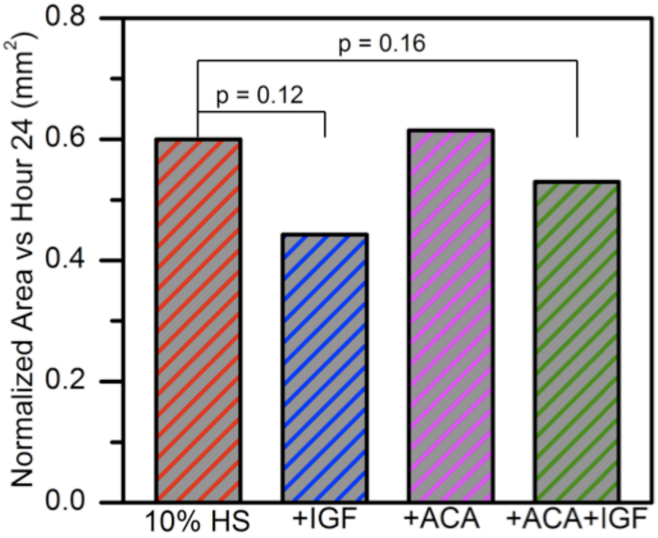

Figure 4.4: Effect of DM Components on Compaction. Addition of IGF-I increased the degree of compaction (i.e., decreased the cross-sectional area more quickly) from hour 24-48.

4.3 DIFFERENTIATION MEDIA COMPONENTS

4.3.1 EFFECT ON MYOTUBE FORMATION

Before adding IGF-I to the DM for the bio-bots, we studied its effect on myoblast differentiation in culture. Although the culture conditions between 2D and 3D culture differ greatly (flat, stiff, tissue culture plastic versus a compliant matrix with room for migration and proliferation), the study provided a basic understanding of how IGF-I would affect the C2C12s, both spatially and temporally. 50 ng/ml IGF-I was added to the dish when myoblasts neared 100% confluency (day 0) and the effect was observed until day 17. For every time point after day 0, the number of myotubes in the samples with IGF-I was significantly increased ($p < 0.05$ or $p < 0.01$) compared to the control (no IGF-I) (**Figure 4.5**). The decrease between day 3 and day 7 can be attributed to additional fusion of cells, which thereby decreased the total number of myotubes. We also hypothesized that the rate of fusion would increase further with a higher concentration of horse serum; therefore, all future experiments were conducted with 10% HS.

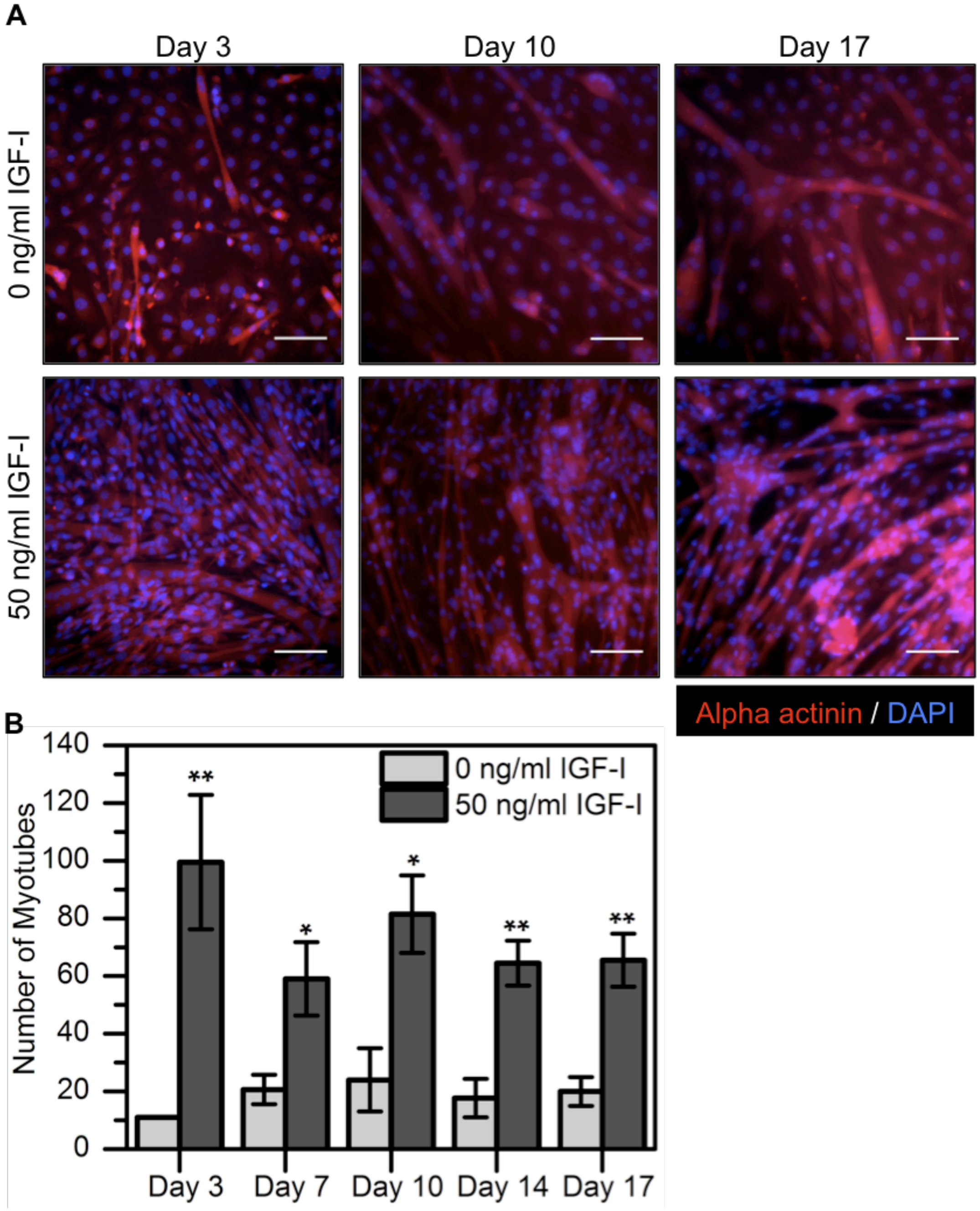

Figure 4.5: Effect Of IGF-I On Myotube Formation. (A) Fluorescent images demonstrating the differentiation and maturation of myotubes in DM(2%HS+IGF) versus DM(2%HS). Scale bar, 100 µm. (B) The number of myotubes was significantly increased for each time point with the addition of IGF-I compared to the control. Values are presented as mean ± SD. Statistics represent one-way ANOVA and Tukey's test, with (*) = $p < 0.05$ and (**) = $p < 0.01$ for $n = 2$-3.

4.3.2 EFFECT ON LIFETIME OF MUSCLE STRIPS

The effect of varying concentrations of HS, IGF-I, and ACA in DM on the lifetime of the bio-bots was studied by monitoring the number of days until the muscle strip ruptured (**Figure 4.6**). No significant difference was observed between DM(2%HS) and DM(10%HS) (8.5 and 8.75 days, respectively). A significant increase (from 8.75 to 25 days, a 185% increase, $p < 0.01$) was observed with the addition of the anti-fibrinolytic agent ACA compared to the DM(10%HS) control. C2C12s can produce plasminogen, which activates plasmin to degrade fibrin; therefore, an anti-fibrinolytic agent was necessary to delay rupture of the muscle strip (Khodabukus & Baar, 2009).

The addition of 50 ng/ml IGF-I decreased the number of days until failure (4.25 days), potentially due to the increased tension within the muscle strip resulting from a greater number of mature myotubes (**Figure 4.5**). Again, adding IGF-I to the media slightly decreased the lifetime compared to DM(10%HS + ACA), but not significantly (from 25 to 19.5 days, a 22% decrease), indicating a more substantial dependence of the muscle strips on degradation than myotube formation. Due to these results, the bio-bots were supplemented with DM(10% HS + ACA + IGF) unless otherwise specified.

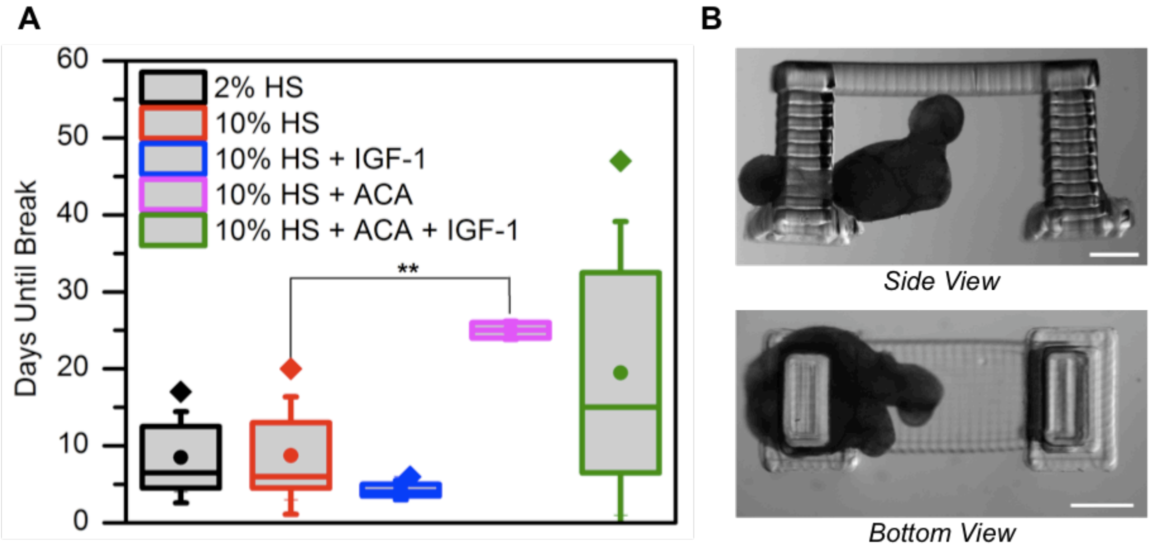

Figure 4.6: Effect of DM Components on Lifetime of Muscle Strips. (A) Boxplot representation of the effect of 50 ng/ml IGF-I, 1 mg/ml aminocaproic acid (ACA), and concentration of horse serum (HS) in differentiation media on the lifetime of the muscle strips (i.e., days until mechanical failure of cell-matrix). Boxes represent 25th, 50th, and 75th percentile; (•) represents mean value; whiskers represent ± SD. Statistical significance represents one-way ANOVA and Tukey's test, with (**) = $p < 0.01$ compared to control (10% HS) for n = 4. (B) The broken muscle strips. Scale bar, 1 mm.

4.4 BENDING AND PASSIVE TENSION

4.4.1 BENDING

As discussed, the energy dose of polymerization from the SLA could be altered to achieve different mechanical properties of the material. The energy dose was varied from 95 to 513 mJ/cm^2 to achieve bio-bots with five distinct bending profiles (**Figure 4.7**). The lowest energy dose resulted in a beam with a lower elastic modulus. This increase in compliance in the less stiff hydrogels provided less resistance to bending; thus a higher deflection in the beam was observed. Conversely, the highest energy dose (513 mJ/cm^2) produced a beam with the highest modulus, and the resulting stiffness created a resistance that the cells could not overcome to move the pillars. Therefore, the bending in the stiffer beam was negligible in comparison.

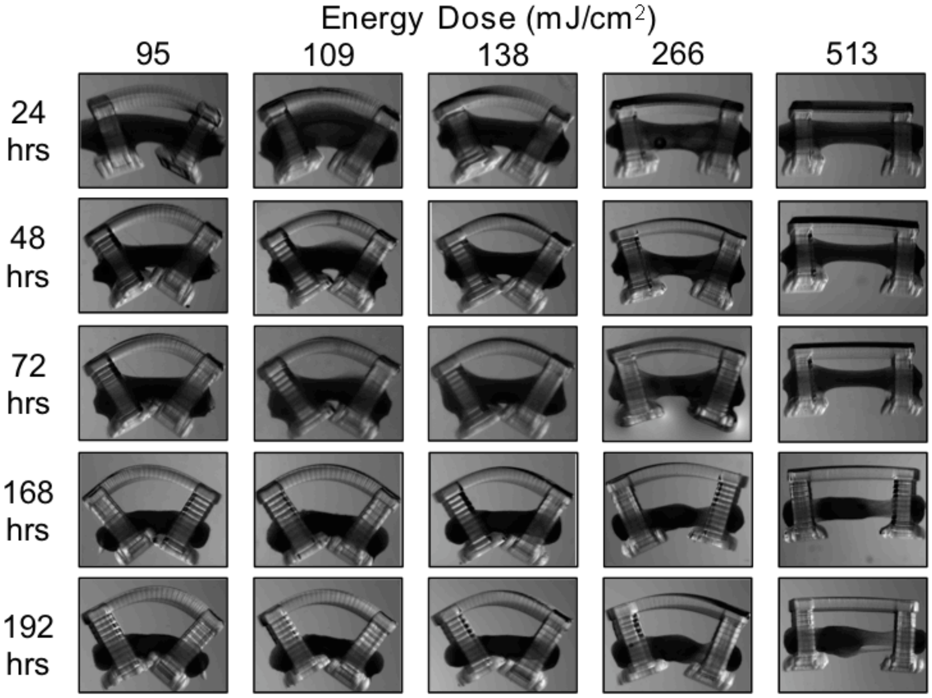

Figure 4.7: Bending with Time and Energy Dose. The polymerization energy from the SLA dictated the mechanical properties of the material. Over time, bio-bots polymerized with different energy doses exhibit different bending profiles in the beam.

4.4.2 PASSIVE TENSION

The passive tension in the muscle strip was analyzed using material properties (elastic modulus of the beam) as well as geometric properties and maximum deflection of the beam from the horizontal (found using an analysis of images shown in **Figure 4.7**). Using the linear bending theory discussed in **Section 3.5.1**, the tension was calculated every 24 hours until the muscle strips broke. Calculation of the tension proved quantitatively what had been observed qualitatively: increasing the energy dose of polymerization resulted in an increased stiffness in the beam that increased the tension in the muscle strip. For energy doses of 95, 109, 138, and 266 mJ/cm^2, the passive tension values were approximately 800, 975, 1035, and 1275 μN, respectively. After stabilizing (i.e., after the first 2-4 days after seeding, during which the compaction and bending continued to increase), the tension remained fairly consistent throughout the lifetime of the muscle strips, with a standard deviation between approximately 4-16 μN depending on the energy dose. The tension (as well as energy dose and elastic modulus) was inversely related to the lifetime of the muscle strips (indicated by an × in **Figure 4.8**). The resistance to bending increased the tension in the matrix of the muscle strip, which could not be sustained long-term. It has been demonstrated that skeletal muscle force output increases under mechanical stimulation and stretching, which explains the increase in passive tension with stiffness (Bach et al., 2004). During myogenesis, mechanical stimulation affects protein expression, gene regulation, and metabolic activity; passive and active forces are both influential in muscle maturation (Goldspink et al., 1992; Powell et al., 2002). Another result of the increased stiffness could be a further degree of alignment within the muscle strip, which is closer to the native organization of functional skeletal muscle, and could also increase the tension (Koning et al., 2009).

Bio-bots incubated in DM without IGF-I, i.e. DM(10%HS + ACA) were compared in order to quantify the effect of IGF-I on the passive tension in the muscle strips. The addition of IGF-I increased the passive tension for the 109 mJ/cm^2 bio-bot from 839.83 ± 11.61 to 962.18 ± 5.16 μN (14.59%) during the observed period when the muscle strips were intact (days 3-16, **Figure 4.9A**). Similarly, the tension in the 138 mJ/cm^2 bio-bot increased from 935.05 ± 6.56 to 1040.87 ± 2.86 μN (11.32%) during the same time period. Consistent with the decreased lifetime observed in bio-bots with the addition of IGF-I (see **Figure 4.6A** above), these bio-bots cultured with IGF-I did not last as long before the muscle strip broke as compared to those without IGF-I (**Figure 4.9B**). These results suggest that the increase in tension with IGF-I (due to an increased number of mature myotubes that are about to displace the pillars with a greater force) adversely affected the lifetime of the muscle strips by creating a tension that could not be sustained.

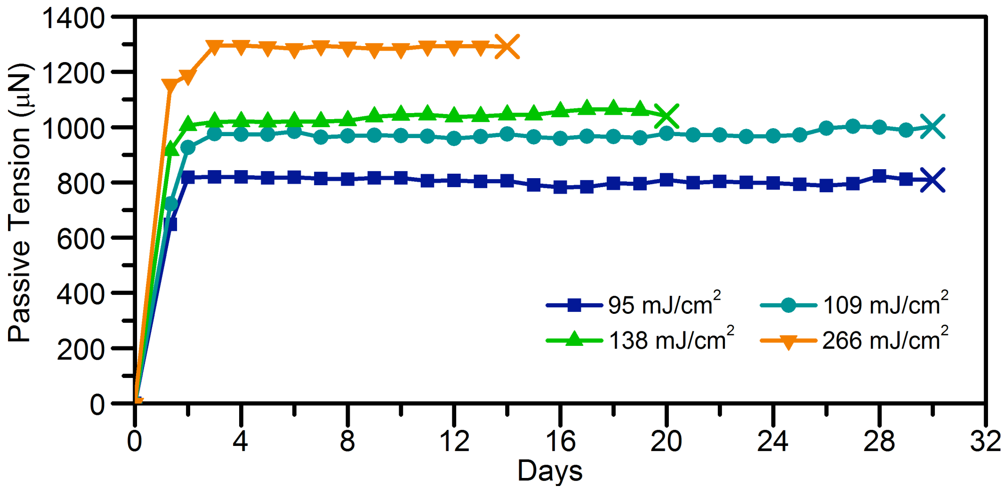

Figure 4.8: Passive Tension. Passive tension in the muscle strip as a function of time and energy dose for n = 2. Increasing the stiffness of the beam resulted in a higher tension and faster time to break (×). *In collaboration with Ritu Raman*.

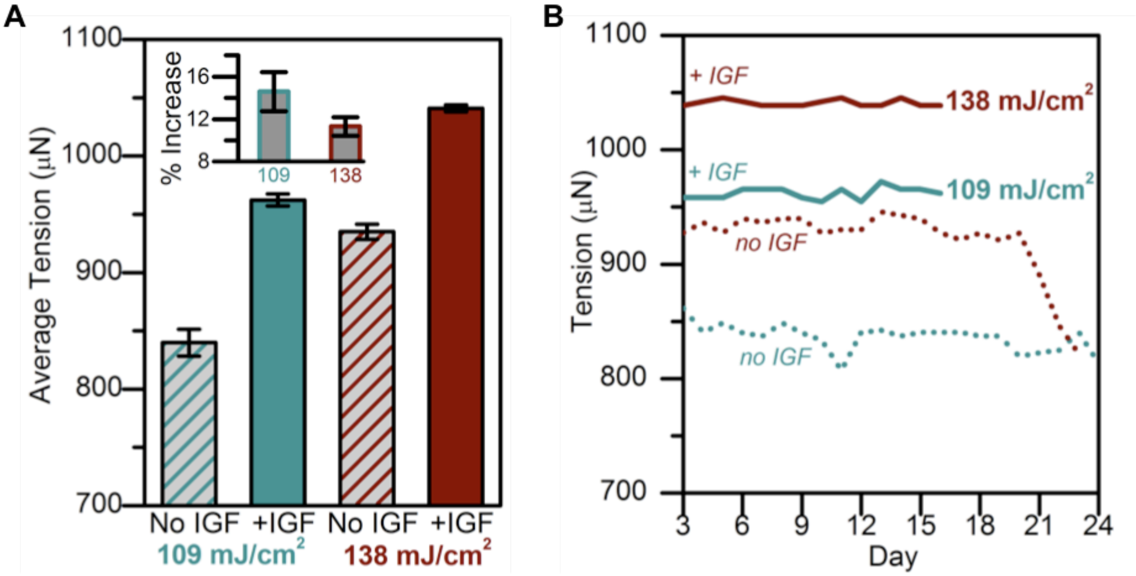

Figure 4.9: Effect of IGF on Passive Tension. (A) Addition of IGF-I to the culture medium increased the average passive tension in the muscle strips between 11-15% compared to the control (no IGF-I). (B) The tension in the muscle strips remained fairly consistent through day 16, but eventually those with IGF-I broke sooner due to the increased tension that could not be sustained. *In collaboration with Ritu Raman*.

4.4.3 ANSYS MODELING AND ERROR

An ANSYS simulation was used to model the global displacement of the beam and pillars using finite element analysis (**Figure 4.10**). Modeling of the design provided another method to "forward engineer" the bio-bot by using known quantities (material properties, elastic modulus, and passive tension) to simulate changes in design parameters and view the resulting bending profile. The resultant global deformation at 192 hours was compared to the original measurement of the deflection of the beam.

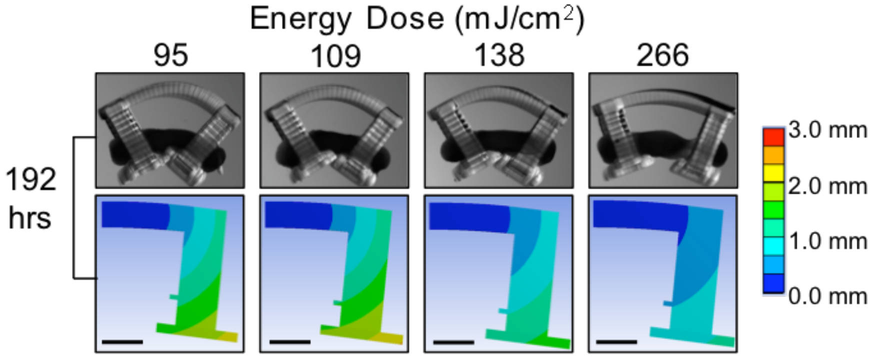

Figure 4.10: Modeling. ANSYS simulation demonstrating global change in displacement of the bio-bot beam and pillars at 192 hours. Scale bar, 1 mm. *In collaboration with Ritu Raman.*

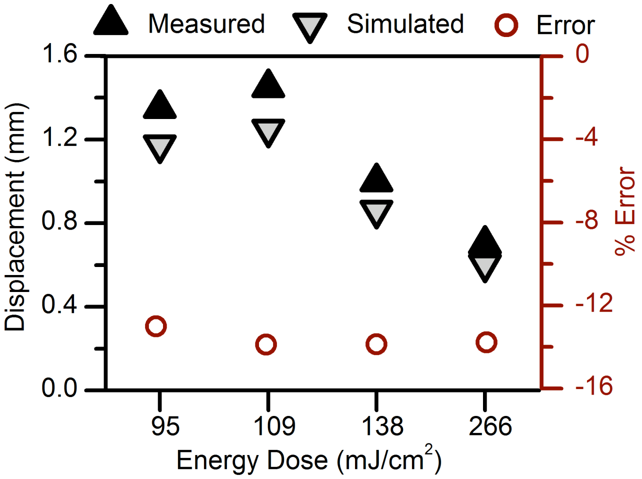

Figure 4.11: Simulation Error. The measured and simulated values of maximum displacement recorded for bio-bots of various energy doses at 192 hours are compared. The values of percent error between the actual and simulated displacements are between 13-14%. *In collaboration with Ritu Raman.*

It was found that the simulation approximated the actual displacement with absolute values of the errors ranging from 13-14%, depending on the energy dose (**Figure 4.11**). As part of an imperfect biological system, this error can be accounted for by several variables, including nonlinear effects (large deformation and rotations), a non-uniform distribution of cells and matrix within the muscle strip, slight non-uniformity and asymmetry in the actual device, and the cases where the bottom caps of the pillars are touching in some bio-bots.

4.5 MATURITY AND FUNCTIONALITY

In order to determine the degree of maturation, alignment, and distribution of the skeletal muscle cells within the muscle strip, the muscle strips were fixed, stained, and imaged with a confocal microscope. Fluorescent markers stained for MF-20, a mature sarcomeric myosin protein, as well as DAPI for the nuclei. Fluorescent analysis also allowed for the examination of the effects of IGF-I on differentiation and maturity.

Figure 4.12 shows the distribution of cells within the matrix with the addition of IGF-I. It is clear from the fluorescence intensity that there are greater numbers of cells around the periphery, most likely due to the limited diffusion of nutrients and oxygen to the cells in the middle of the muscle strip. The alignment of some cells around the border could be attributed to the tension in this direction. Myotubes can be identified by their length (in contrast to rounder myoblast) and multiple nuclei.

Figure 4.13 depicts the arrangement of muscle cells within a muscle strip without IGF-I. Although multinucleated myotubes are visible (see **Figure 4.13** inset), there are fewer throughout the matrix than in the muscle strips with IGF-I, confirming the role of IGF-I in increasing the rate of myogenesis. **Figure 4.13D** demonstrates the presence of myotubes along with many myoblasts. The density of myotubes is not as great as those seen with IGF-I in **Figure 4.12C-D**. Further fluorescent imaging at different time points could confirm this hypothesis with a quantitative analysis of maturation and cell number.

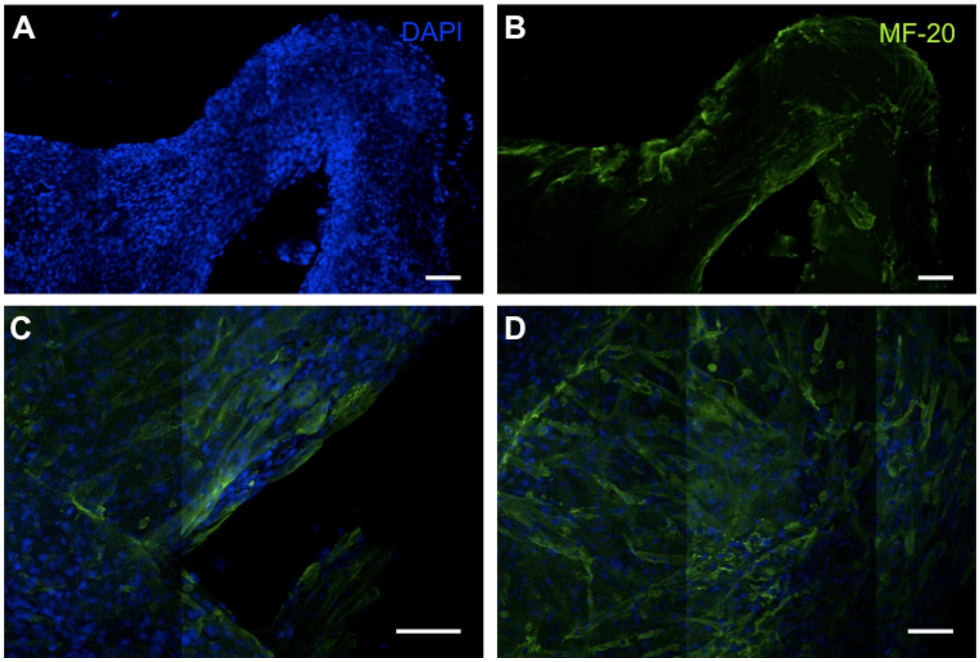

Figure 4.12: Confocal Imaging with IGF-I. (A) DAPI nuclear stain of region of muscle strip. (B) MF-20 myosin sarcomere stain of same region of muscle strip. (C) The density and alignment of myotubes are visible along the edge of the muscle strip. (D) Myotubes within the muscle strip. Scale bar, 100 µm (all).

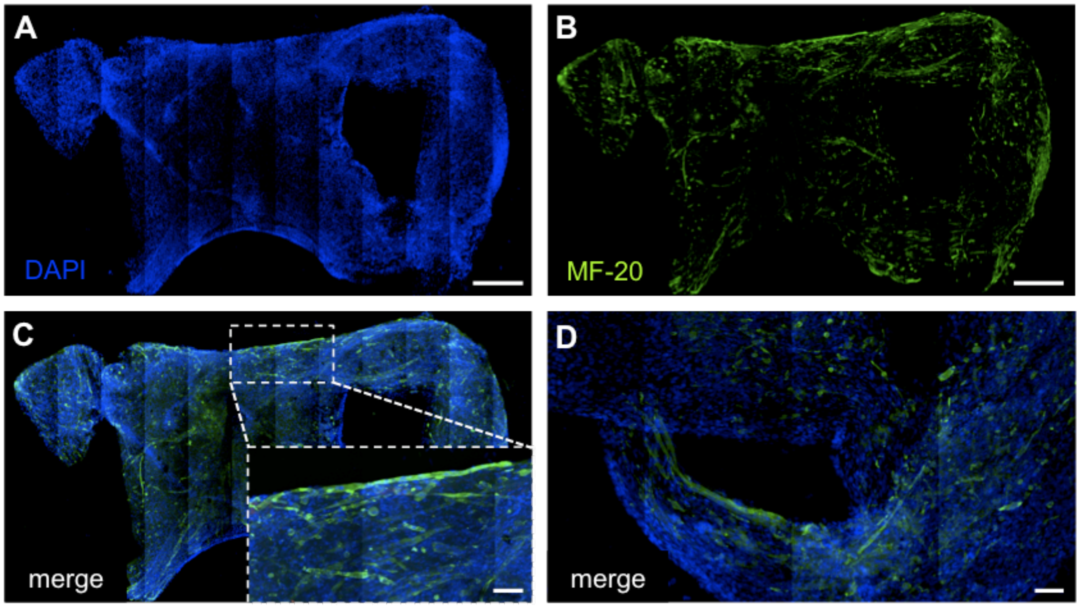

Figure 4.13: Confocal Imaging without IGF-I. (A) DAPI nuclear stain of entire muscle strip. (B) MF-20 myosin sarcomere stain of entire muscle strip. Scale bar, 500 µm (A,B). (C) Merged image; inset, myotube along muscle strip perimeter. (D) Detail of cell organization and maturity. Scale bar, 100 µm (C,D).

4.6 SPONTANEOUS LOCOMOTION

4.6.1 NET DISPLACEMENT

After 15 days, the muscle strips of three 109 and 138 mJ/cm^2 bio-bots incubated in DM(10%HS + ACA + IGF) began spontaneously twitching. An adequate number of cells in the muscle strip were contracting to move the pillars a discernible distance with each twitch. A camcorder was used to track the movement of the three bio-bots (hereafter referred to as 109, 138-1, and 138-2) across the surface of the tissue culture dish for observation periods ranging from 5-10 minutes (**Figure 4.14A**).

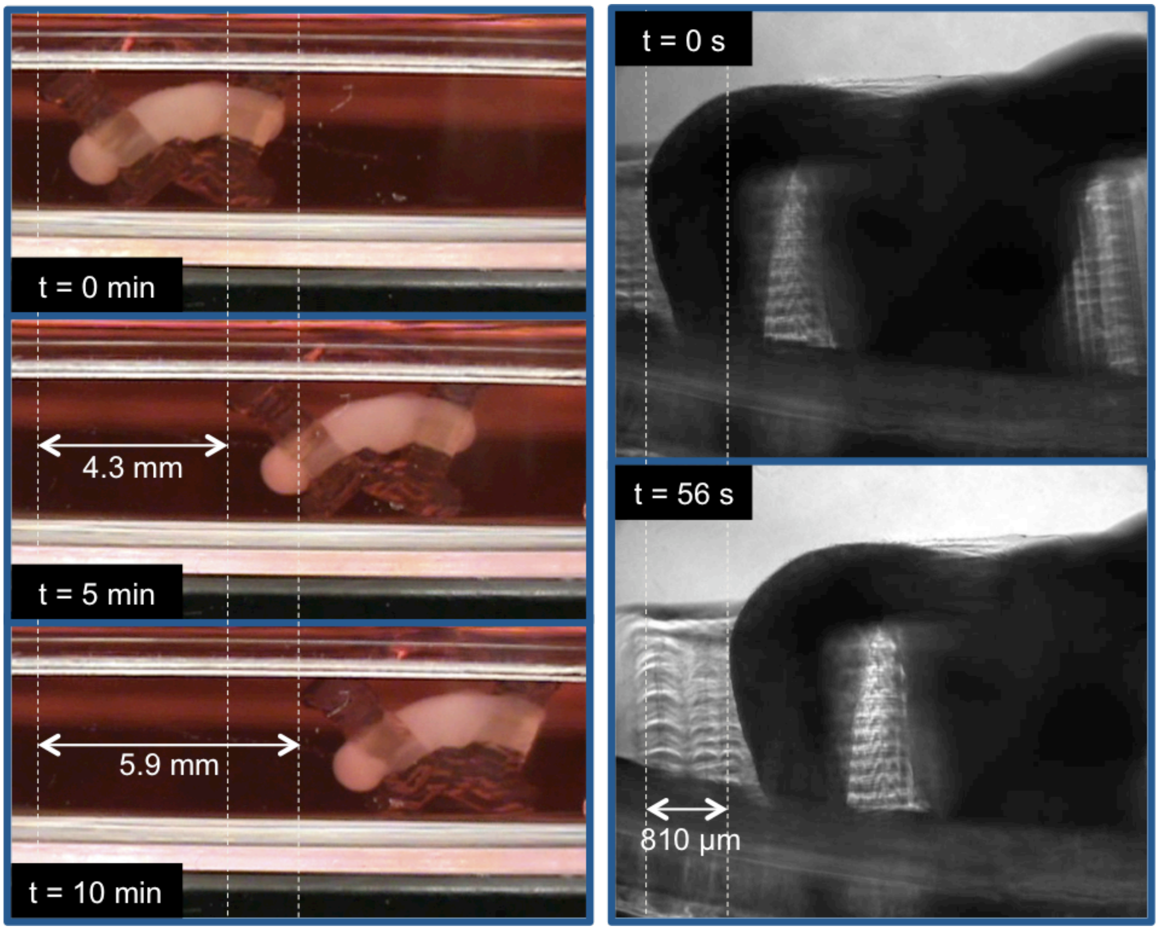

Figure 4.14: Net locomotion. Camcorder (left, side-view) and microscope (right, top-view) images of the bio-bots moving across a surface due to spontaneous twitching of cells within the muscle strip.

All three bio-bots achieved net locomotion on days 15 and 16. The muscle strips from 109 and 138-1 broke after day 16, and the remaining measurements (days 17-19) are from 132-2 (which broke before imaging could be done on day 20) (**Figure 4.15**). Interestingly, all of the bio-bots displaced a greater distance per minute at later time points, likely due to increased maturation and force production capability of the cells within the muscle strip. No spontaneous twitching or net displacement was observed without IGF-I, i.e. from bio-bots cultured in DM(10%HS + ACA) through day 30; it is hypothesized that the myotubes in these muscle strips lagged behind those cultured with IGF-I in terms of maturation.

Spontaneous contraction of differentiated skeletal muscle has been observed in many engineered muscle constructs, especially with the use of C2C12s. In many cases has been noted in the days following the addition of differentiation medium, and increased in the days thereafter (and generally after replacing the medium) (Bian & Bursac, 2009; Dennis et al., 2001; Hinds et al., 2011; Kosnik et al., 2001; Liao & Zhou, 2009; Sakar et al., 2012). However, skeletal muscle, unlike cardiac or smooth muscle tissue, requires stimulus from a neuromuscular junction and does not inherently contract within the body. An action potential stimulates the release of calcium ions from the sarcoplasmic reticulum (SR), resulting in contraction until the active removal of calcium into the SR (Marieb, 2006). It is possible that the myotubes reached a state of early deterioration during the observation process (days 15-19) with increased intracellular calcium that resulted in spontaneous contraction after this time point. The integration of optogenetic regulation earlier in the differentiation process will allow a greater level of control over myotube contraction and movement of the bio-bot (see **Section 5.1**).

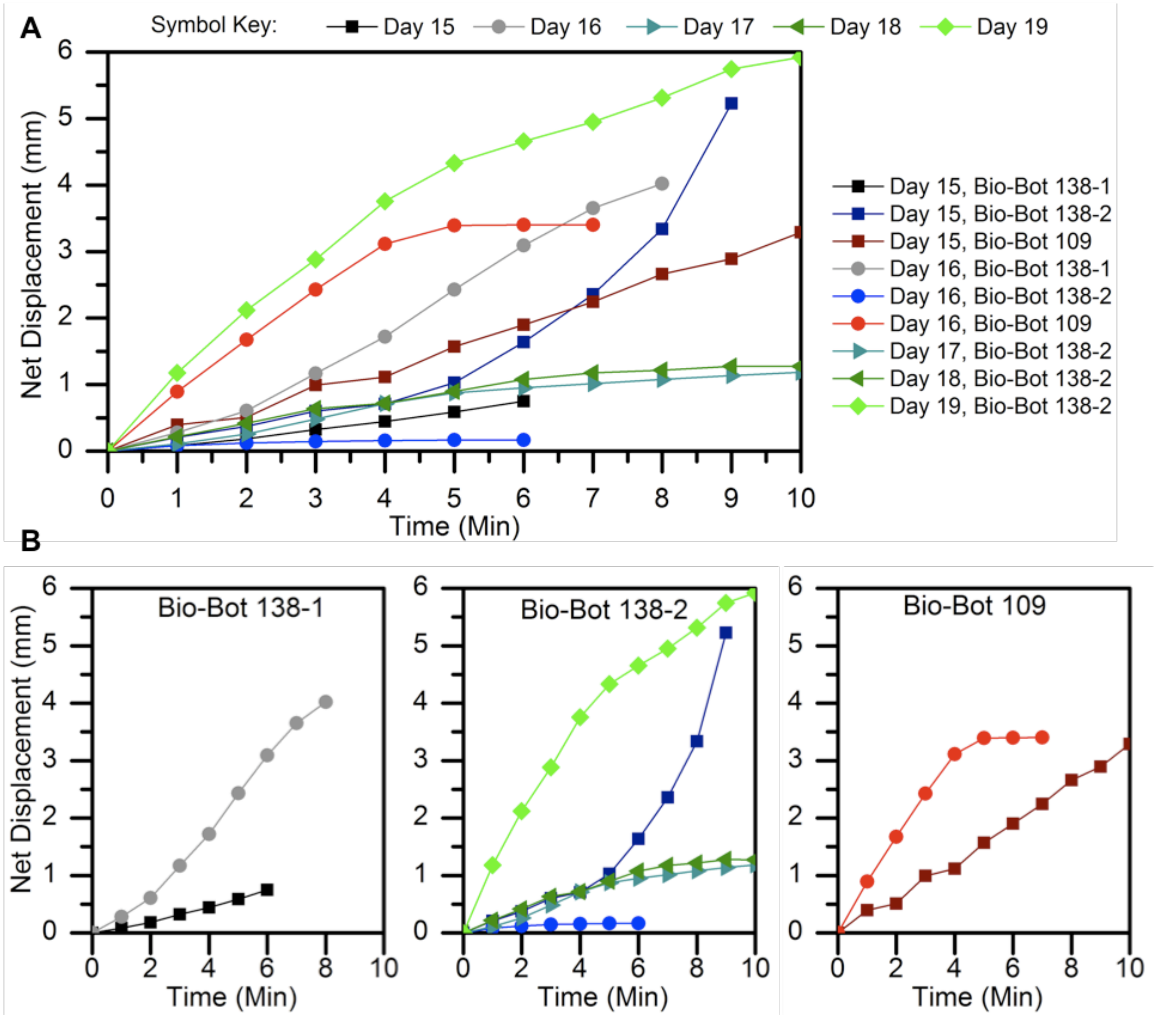

Figure 4.15: Net displacements. (A) Net displacements of all bio-bots (109, 138-1, and 138-2) over an observation period of 5-10 minutes from days 15-19. (B) Net displacements observed for each bio-bot individually. Generally, greater displacement per minute was observed at later time points.

4.6.2 VELOCITY

To determine the velocities of the actuating bio-bots, still frames from each minute of observed locomotion were overlaid and the displacements were divided by the time interval. Average velocity was calculated as total displacement during observation divided by the total time of observation (**Figure 4.16A**). Maximum velocity was calculated with the maximum value of all distances traveled within a minute's time (**Figure 4.16B**). As with the values of displacement, large variation can be seen in the velocities of the bio-bots, both across devices and over time. Although measurement conditions were kept as constant as possible, lack of consistency can be attributed to differences in cell distribution, temperature of the medium, and a geometric imbalance that prevented the force of contraction from overcoming the friction of the dish. The bio-bot was fabricated as a symmetric design, but its asymmetry evolved over time due to non-uniform distribution of cells within the muscle strip. Improvements and future designs are discussed in Chapter 5.

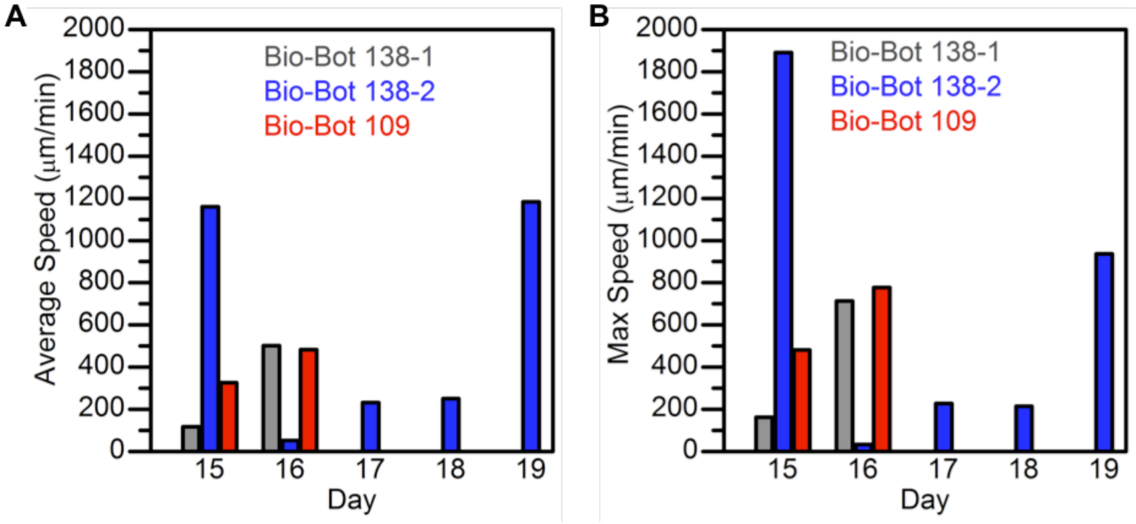

Figure 4.16: **Average and Maximum Velocities.** (A) Average speed (μm/min) of spontaneous actuating bio-bots from days 15-19. Bio-bot 138-2 continued to contract for three days after the muscle strips in 138-1 and 109 broke. (B) Maximum velocities (μm/min) observed during one-minute intervals for actuating bio-bots. Inconsistency can be attributed to differences in cell distribution, temperature of the medium, and asymmetry that prevented the force of contraction from overcoming the friction of the dish.

4.6.3 FREQUENCY OF CONTRACTION

The frequency of contractions was observed for bio-bot 138-2 on days 18 and 19 by counting the number of visible contractions during 1-minute time intervals. (Note that this quantity does not represent individual myotube contractions, which could not be discerned using this method, but rather a sum of local contractions that globally produced enough force to move the pillars of the structure.) An approximate inverse relationship can be observed between the displacement and frequency (**Figure 4.17**). On both days, as the displacement increased, the frequency of contractions generally decreased. Although fresh warm (37ºC) media was added to each dish before recording started, it is likely that the temperature decreased below a physiological range over the span of 5-10 minutes. Recording the movement in a temperature-controlled chamber would eliminate this issue.

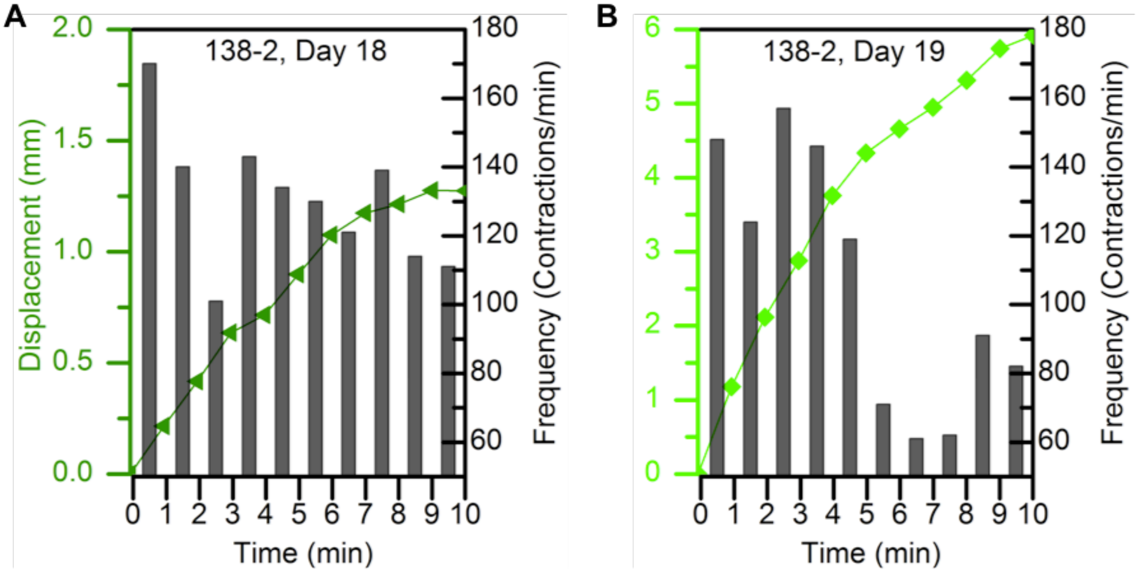

Figure 4.17: Frequency of Contraction. (A) Net displacement and frequency (contractions per minute) of bio-bot 138-2 on day 18. (B) Net displacement and frequency (contractions per minute) of bio-bot 138-2 on day 19. The average observed frequency decreased, although the net displacement increased. Note the different scales of displacement values between (A) and (B).

5. CONCLUSIONS AND FUTURE DIRECTIONS

5.1 OPTOGENETIC CONTROL

Over the past decade, a new method has harnessed the power of genetics and engineering to achieve cellular control. Engineers and biologists have turned to optogenetics ("Method of the Year" by Nature Methods in 2010, with over 23,000 citations to date) as a remarkable and powerful cell perturbation tool (Entcheva, 2013). In addition to offering fast control over precisely defined events in a defined and targeted manner, optogenetics allows for cell-specific control with precise spatial and temporal targeting of biological systems in a reversible and non-invasive manner. No exogenous chemical is required, and many of the harmful consequences of electrical stimulation are eliminated (Deisseroth, 2012; Rein & Deussing, 2012). We plan to use optogenetics in order to achieve control over the movement, pacing, and directionality of the bio-bots.

The basis of optogenetic stimulation is the introduction of gain or loss of function of precisely defined events in a cell. These events are achieved through light-responsive ion channels called rhodopsins. Microbes lack complex eye structures; therefore, they have developed the use of light-activated rhodopsin proteins to respond to stimuli and maintain homeostatic balance. Rhodopsins are found in all kingdoms of life and are characterized by their "unitary nature:" a single gene encodes both the light-sensing and effector (ion flux) domains of the molecule (Fenno et al., 2011; Zhang et al., 2011). The formation of a functional rhodopsin complex requires retinal (a co-factor) to bind an opsin protein (**Figure 5.1A**). Binding of a photon results in isomerization and a subsequent conformational change of the opsin from *trans* to *cis*, enabling an ionic flow. The relative availability of retinal chromophores in vertebrate cells eliminates the need for an exogenous molecule to activate the ion channel (Pastrana, 2010).

Channelrhodopsins are sensory photoreceptors with seven trans-membrane helical regions and a channel characterized by charged amino acid residues (Watanabe et al., 2012). Channelrhodopsin-2 (ChR2) is a non-selective cation channel that responds to blue light (~480 nm) activation by permitting a passive influx of positive ions along a membrane gradient (**Figure 5.1B**). The subsequent depolarization of the cell (increase in voltage above the threshold for action potential generation) results in a "gain of function" event (Fenno et al., 2011). ChR2 has a low selectivity among positive anions, but is not “unspecific” because it does not permit the conductance of anions across the membrane.

The C2C12 skeletal muscle myoblasts used in this study have been transfected with ChR2. Preliminary experiments have shown contraction of the cells in response to blue light stimulation (data not shown). By selectively exciting the ChR2 C2C12s, the movement and pacing of the bio-bot could be achieved in a controlled manner. We believe this would also allow for earlier control in the lifetime of the muscle strips, i.e., before spontaneous contraction has been observed.

Optogenetic tools can easily be delivered with viral gene transfer mechanisms (adeno-associated viruses and lentiviruses) or transgenic animal lines. In 2005, Boyden, Deisseroth and colleagues used ChR2 to stimulate rat neurons in the first demonstration that opsins could generate sufficient photocurrents for control of mammalian cells through membrane depolarization. The researchers also determined that expression of ChR2 did not alter the membrane characteristics or overall health of the cells (Boyden et al., 2005).

Reports of optogenetic muscle cells have lagged behind neuroscientific studies by about half a decade. Optogenetic control of heart muscle was achieved by Bruegmann *et al*. with a transgenic mouse embryonic stem cell (ESC) line that expressed a mutant form of ChR2 differentiated through the formation of embryoid bodies (EBs) to form cardiomyocytes. Optical stimulation of one region of a ChR2-expressing cardiomyocyte layer was followed by activity in other regions through spreading of the electrical signal across cell junctions, demonstrating the potential of a pacemaker site. Finally, transgenic mice with ventricular cardiomyocytes expressing ChR2 were intubated and the beating hearts were illuminated with blue light. An ECG recorded supraventricular pacing of the heart in response to the pulsed optical stimulation. Traditional electrical stimulation of cardiac muscle is irreversibly damaging, inhomogeneous, and unable to induce lengthy depolarizations (Bruegmann et al., 2010). Arrenberg and colleagues expressed ChR2 and NpHR in zebrafish cardiomyocytes to stimulate various cardiac events such as tachycardia, atrioventricular blocks, and cardiac arrest. Contractions were almost instantaneously blocked by NpHR stimulation and reversibly recovered when the illumination was removed (Arrenberg et al., 2010).

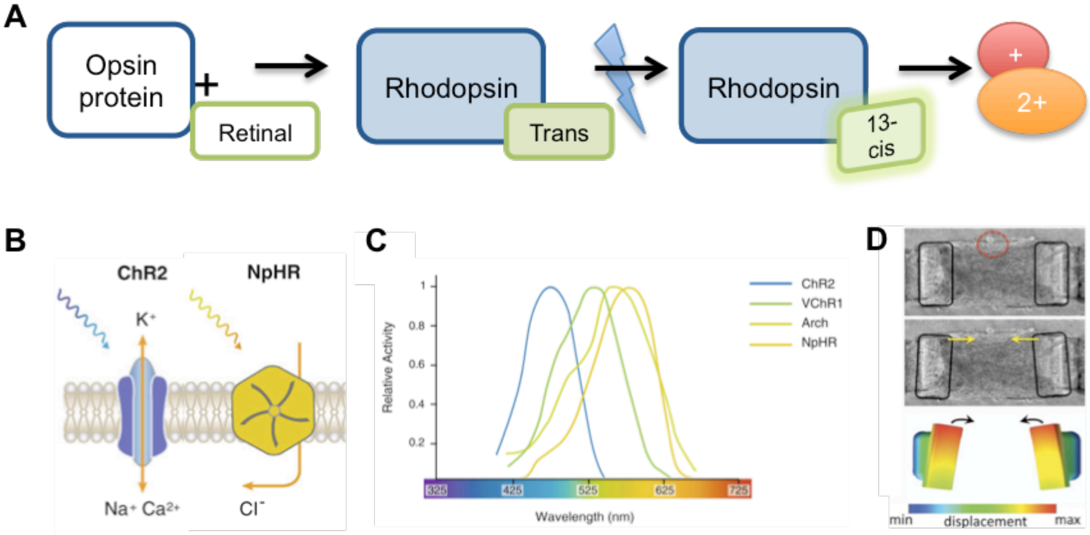

Figure 5.1: Optogenetics. (A) An opsin protein binds the co-factor retinal to become all-*trans* rhodopsin. Photon absorption induces a conformational change to a *cis* formation, and an ionic flow is established across the membrane. (B) & (C) Various rhodopsins have a range of spectral profiles permit the flow of positive and negative ions (Rein et al, 2012) (D) Displacement of a pair of cantilevers surrounded by optogenetic C2C12s is controlled by the cells' response to blue light (Sakar et al., 2012)

Asano and colleagues published one of the first reports of photosensitive skeletal muscle cell control. A blue-light LED with a power density of 0.12 mW/mm^2 was used to optically stimulate ChR2-transfected C2C12 myotubes in one of the first. A muscle cell twitch was observed for pulses at frequencies between 1-4 Hz; above 5Hz, the effect varied among myotubes. For some myotubes, however, no amount of stimulation strength could induce an action potential (Asano et al., 2012). Sakar *et al*. seeded ChR2-expressing C2C12s into PDMS microwells with collagen and Matrigel, applied 20 ms blue light pulses, and measured the displacement of attached cantilevers. This method demonstrated not only a novel bioactuator technology but also the ability to control its stimulation and movement in a specific manner (**Figure 5.1D**, **Section 2.4.3**) (Sakar et al., 2012).

Halorhodopsin is structurally homologous to ChR2, but fundamentally different in its working principle. In contrast to channelrhodopsins, halorhodopsins are chloride pumps that inhibit an action potential (**Figure 5.1B**). Influx of negative ions into induces hyperpolarization of the membrane (and subsequent silencing of the cell) with yellow light activation (~589 nm). Halorhodopsin must work against an electrochemical gradient to pump ions across the membrane (Rein & Deussing, 2012). Zhang and members of the same team combined ChR2 with a halorhodopsin chloride pump (NpHR) sensitive to yellow light). Addition of this hyperpolarizing ion channel allowed for an inhibition to complement ChR2 in a multimodal, bi-directional targeting system of neuronal circuits. The spectral separation between ChR2 and NpHR (~100 nm) allowed the two events to be conducted separately or together. Fusion of ChR2/NpHR was examined in body wall muscles of a transgenic nematode (*C. elegans*), with NpHR effectively countering the activity from ChR2 (Zhang et al., 2007). Eventually, we desire to achieve multimodal ON/OFF control of C2C12-based bio-bots with the incorporation of NpHR as well as ChR2. The bio-bot could be stimulated to begin contracting with blue light, and forced to halt with yellow light.

5.2 OPTIMIZATION AND BIO-INSPIRED DESIGNS

The current design of the bio-bot does not permit optimized locomotion due to many factors. The first is the geometric set-up. Although inherently asymmetric due to a non-uniform distribution of cells within the muscle strip and unbalanced placement of the pillars, the original design assumes a balanced arrangement of muscle strip surrounding equidistant pillars. The proof-of-concept design was inspired by published reports of micro-tissue cantilever force measurement devices (Boudou et al., 2012; Sakar et al., 2012). Therefore, the introduction of deliberate asymmetry (either by extending the length of one of the pillars or ensuring localization of skeletal muscle cells on one side of the muscle strip) would likely result in greater displacements and velocities of the device across a surface.

Additionally, the incorporation of multiple muscle strips into a “multi-legged” design (with each “leg” comprised of a muscle strip surrounding two pillars) would allow for directional control over the bio-bot’s movement. Blue-light stimulation of one “leg” would result in displacement in a specified direction; the bio-bot could change directions with the application of blue light to an opposing “leg” (**Figure 5.2**).

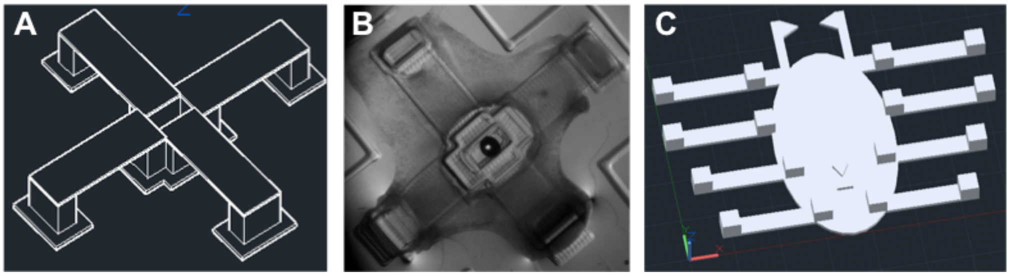

Figure 5.2: Multi-legged designs. (A) AutoCAD rendering of 4-legged bio-bot. (B) Actual image of muscle strip compaction around 4-legged bio-bot. (C) AutoCAD rendering of "spider" 8-legged device.

Finally, the output of the bio-bot could be improved by improving the organization and functionality of the skeletal muscle. Despite the recent advances in this field, some challenges remain: first, the fabrication of muscle tissue that exhibits proper alignment and architecture, i.e. myofibers that are densely arranged and aligned in a large volume. Lam *et al*. devised a method to develop pre-aligned muscle constructs by patterning topographical features on a PDMS substrate. Myoblasts were seeded on the PDMS surface, differentiated, and covered with a tin layer of fibrin. The cells self-organized by rolling up into 3D constructs and began to degrade the fibrin matrix over time. The functional force production from aligned constructs was more than doubled compared to the unaligned control (Lam et al., 2009). A method to increase alignment in the muscle strips would most likely increase the force production and net locomotion of the device.

Depriving metabolic tissues of nutrients and oxygen can lead to necrosis on the inside of the tissue (i.e., more than couple of hundred microns from the edge), as fluorescent imaging has demonstrated. The use of hydrogels as a support platform can help to alleviate some issues, as they can provide an environment compatible with cell alignment and organization (Bian & Bursac, 2008; Khodabukus & Baar, 2009). Fibrin is a natural hydrogel, but perhaps the composition of the matrix can be optimized to find the conditions that allow for the metabolic needs of the tissue.

5.3 MICROSTEREOLITHOGRAPHY SYSTEM

A micro-stereolithography system is currently being developed for two purposes: first, creating bio-bots with smaller features, and second, as a platform for selectively stimulating individual cells or cell clusters within the muscle strip. Micro-stereolithography is a “top-down” fabrication approach that uses a projected light system and a digital micro-mirror device (DMD) or liquid crystal display (LCD) as a dynamic mask (Cho & Kang, 2012). A DMD is an array of individual micro-mirrors that can be switched on or off for every pixel. In contrast to traditional stereolithography, re-coating of the surface is not necessarily required, the illuminated surface is smooth, and oxygen inhibition is limited because the layer being polymerized is not in contact with the atmosphere (Melchels et al., 2010). The yield is increased by a decreased fabrication time; instead of using a scanning laser, the entire layer is cured at once by the projection of a 2D pattern onto a transparent platform.

Light for optogenetic stimulation can be delivered through filtered mercury lamps, lasers, LEDs or LED arrays (for multi-site stimulation), as well as optical fibers transmitting laser light through cannulas for *in vivo* studies. A DMD or two-photon confocal microscope can be used to control the pattern of light on specific cells or regions to selectively stimulate a subset of excitable cells or part of the cells (Fenno et al., 2011; Pastrana, 2010). Manipulation of light on a millisecond-scale light (a range relevant for action potentials and other events of excitable cells) is required, and Zhang *et al*. reported a minimum power density of 5-12 mW/mm^2 for photoactivation (Zhang et al., 2006).

5.4 A COMPLETE CELLULAR SYSTEM

The integration with other cell types and subsequent vascularization for long-term survival and metabolic activity is necessary to sustain muscle cell contraction. The critical interfaces of skeletal muscle are myotendious (mechanical), vascular (chemical), and neuromuscular (sensory and control).

The “biological parts” comprising many higher-level systems have been assembled to date as individual machine components with one or two cell types. Muscle cells have been used for biological actuators and neurons or neuronal networks assemble into sensory clusters or processors. The challenge, then, is to coordinate the cell types in a way that allows for new functionalities and applications in various fields. A complete cellular system needs many different components in order to be self-sustaining and autonomous: muscle cells that allow for movement, neuromuscular junctions to interface between muscle and neurons for control and processing, a vasculature supported by endothelial cells to provide nutrients and oxygen, and an exoskeleton for long-term viability and protection.

Integration of muscle, nature’s own actuator, with optogenetic control, a wireless driver of functional outputs, would truly create a biological “machine”. The addition of other cell types for these functional characteristics will only further define the biological machines of the future.

6. REFERENCES

Arcaute, K., Mann, B. K., & Wicker, R. B. (2006). Stereolithography of three-dimensional bioactive poly(ethylene glycol) constructs with encapsulated cells. *Annals of Biomedical Engineering*, *34*(9), 1429–41. doi:10.1007/s10439-006-9156-y

Arcaute, K., Mann, B. K., & Wicker, R. B. (2011). Practical Use of Hydrogels in Stereolithography for Tissue Engineering Applications. In P. J. Bártolo (Ed.), *Stereolithography: Materials, Processes and Applications* (pp. 299–331). Boston, MA: Springer US. doi:10.1007/978-0-387-92904-0

Arcaute, K., Mann, B., & Wicker, R. (2010). Stereolithography of spatially controlled multi-material bioactive poly(ethylene glycol) scaffolds. *Acta Biomaterialia*, *6*(3), 1047–54. doi:10.1016/j.actbio.2009.08.017

Arrenberg, A. B., Stainier, D. Y. R., Baier, H., & Huisken, J. (2010). Optogenetic control of cardiac function. *Science*, *330*(6006), 971–974. doi:10.1126/science.1195929

Asano, T., Ishizua, T., & Yawo, H. (2012). Optically controlled contraction of photosensitive skeletal muscle cells. *Biotechnology and Bioengineering*, *109*(1), 199–204. doi:10.1002/bit.23285

Bach, A. D., Beier, J. P., Stern-Straeter, J., & Horch, R. E. (2004). Skeletal Muscle Tissue Engineering. *Journal of Cellular and Molecular Medicine*, *8*(4), 413–422.

Bach, T. L., Barsigian, C., Chalupowicz, D. G., Busler, D., Yaen, C. H., Grant, D. S., & Martinez, J. (1998). VE-Cadherin Mediates Endothelial Cell Capillary Tube Formation in Fibrin and Collagen Gels. *Experimental Cell Research*, *238*(2), 324–334.

Bajaj, P., Chan, V., Jeong, J. H., Zorlutuna, P., Kong, H., & Bashir, R. (2012). 3-D biofabrication using stereolithography for biology and medicine. *Engineering in Medicine and Biology Society (EMBC), 2012 Annual International Conference of the IEEE* (Vol. 2012, pp. 6805–8). doi:10.1109/EMBC.2012.6347557

Bártolo, P. J. (2011). Stereolithographic Processes. In P. J. Bártolo (Ed.), *Stereolithography: Materials, Processes and Applications* (pp. 1–36). Boston, MA: Springer US. doi:10.1007/978-0-387-92904-0

Barton, E. R., Morris, L., Musaro, A., Rosenthal, N., & Sweeney, H. L. (2002). Muscle-specific expression of insulin-like growth factor I counters muscle decline in mdx mice. *The Journal of Cell Biology*, *157*(1), 137–48. doi:10.1083/jcb.200108071

Barton-Davis, E. R., Shoturma, D. I., Musaro, A., Rosenthal, N., & Sweeney, H. L. (1998). Viral mediated expression of insulin-like growth factor I blocks the aging-related loss of skeletal muscle function. *Proceedings of the National Academy of Sciences of the United States of America*, *95*(26), 15603–7.

Beier, J. P., Stern-Straeter, J., Foerster, V. T., Kneser, U., Stark, G. B., & Bach, A. D. (2006). Tissue engineering of injectable muscle: three-dimensional myoblast-fibrin injection in the syngeneic rat animal model. *Plastic and Reconstructive Surgery*, *118*(5), 1113–21. doi:10.1097/01.prs.0000221007.97115.1d

Bensaïd, W., Triffitt, J. ., Blanchat, C., Oudina, K., Sedel, L., & Petite, H. (2003). A biodegradable fibrin scaffold for mesenchymal stem cell transplantation. *Biomaterials*, *24*(14), 2497–2502. doi:10.1016/S0142-9612(02)00618-X

Bertsch, A., & Renaud, P. (2011). Microstereolithography. In P. J. Bártolo (Ed.), *Stereolithography: Materials, Processes and Applications* (pp. 81–112). Boston, MA: Springer US. doi:10.1007/978-0-387-92904-0

Bian, W., & Bursac, N. (2008). Tissue engineering of functional skeletal muscle: challenges and recent advances. *IEEE Engineering in Medicine and Biology Magazine*, *27*(5), 109–113.

Bian, W., & Bursac, N. (2009). Engineered skeletal muscle tissue networks with controllable architecture. *Biomaterials*, *30*(7), 1401–12. doi:10.1016/j.biomaterials.2008.11.015

Bian, W., Juhas, M., Pfeiler, T. W., & Bursac, N. (2012). Local Tissue Geometry Determines Contractile Force Generation of Engineered Muscle Networks. *Tissue Engineering: Part A*, *18*(9-10), 957–967. doi:10.1089/ten.tea.2011.0313

Bian, W., Liau, B., Badie, N., & Bursac, N. (2009). Mesoscopic hydrogel molding to control the 3D geometry of bioartificial muscle tissues. *Nature protocols*, *4*(10), 1522–34. doi:10.1038/nprot.2009.155

Boland, T., Tao, X., Damon, B. J., Manley, B., Kesari, P., Jalota, S., & Bhaduri, S. (2007). Drop-on-demand printing of cells and materials for designer tissue constructs. *Materials Science and Engineering: C*, *27*(3), 372–376. doi:10.1016/j.msec.2006.05.047

Boudou, T., Legant, W. R., Mu, A., Borochin, M. A., Thavandiran, N., Radisic, M., Zandstra, P. W., et al. (2012). A Microfabricated Platform to Measure and Manipulate the Mechanics of Engineered Cardiac Microtissues. *Tissue Engineering: Part A*, *18*(9 and 10), 910–919. doi:10.1089/ten.tea.2011.0341

Boyden, E. S., Zhang, F., Bamberg, E., Nagel, G., & Deisseroth, K. (2005). Millisecond-timescale, genetically targeted optical control of neural activity. *Nature Neuroscience*, *8*(9), 1263–8. doi:10.1038/nn1525

Bruegmann, T., Malan, D., Hesse, M., Beiert, T., Fuegemann, C. J., Fleischmann, B. K., & Sasse, P. (2010). Optogenetic control of heart muscle in vitro and in vivo. *Nature Methods*, *7*(11), 897–900. doi:10.1038/nmeth.1512

Bruns, H., Kneser, U., Holzhüter, S., Roth, B., Kluth, J., Kaufmann, P. M., Kluth, D., et al. (2005). Injectable liver: a novel approach using fibrin gel as a matrix for culture and intrahepatic transplantation of hepatocytes. *Tissue Engineering*, *11*(11/12), 1718–26. doi:10.1089/ten.2005.11.1718

Buckingham, M., Bajard, L., Chang, T., Daubas, P., Hadchouel, J., Meilhac, S., Montarras, D., et al. (2003). The formation of skeletal muscle: from somite to limb. *Journal of Anatomy*, *202*(1), 59–68.

Chan, V., Collens, M. B., Jeong, J. H., Park, K., Kong, H., & Bashir, R. (2012). Directed cell growth and alignment on protein-patterned 3D hydrogels with stereolithography. *Virtual and Physical Prototyping*, *7*(3), 219–228. doi:10.1080/17452759.2012.709423

Chan, V., Jeong, J. H., Bajaj, P., Collens, M. B., Saif, T., Kong, H., & Bashir, R. (2012). Multi-material bio-fabrication of hydrogel cantilevers and actuators with stereolithography. *Lab on a Chip*, *12*, 88–98. doi:10.1039/c1lc20688e

Chan, V., Park, K., Collens, M. B., Kong, H., Saif, T. A., & Bashir, R. (2012). Development of Miniaturized Walking Biological Machines. *Scientific Reports*, *2*, 1–8. doi:10.1038/srep00857

Chan, V., Zorlutuna, P., Jeong, J. H., Kong, H., & Bashir, R. (2010). Three-dimensional photopatterning of hydrogels using stereolithography for long-term cell encapsulation. *Lab on a Chip*, *10*, 2062–2070. doi:10.1039/c004285d

Chiron, S., Tomczak, C., Duperray, A., Lainé, J., Bonne, G., Eder, A., Hansen, A., et al. (2012). Complex interactions between human myoblasts and the surrounding 3D fibrin-based matrix. *PloS One*, *7*(4), 1–8. doi:10.1371/journal.pone.0036173

Cho, D.-W., & Kang, H.-W. (2012). Microstereolithography-Based Computer-Aided Manufacturing for Tissue Engineering. In M. A. K. Liebschner (Ed.), *Computer-Aided Tissue Engineering* (Vol. 868, pp. 341–356). Totowa, NJ: Humana Press. doi:10.1007/978-1-61779-764-4

Clemmens, J., Hess, H., Doot, R., Matzke, C. M., Bachand, G. D., & Vogel, V. (2004). Motor-protein "roundabouts": microtubules moving on kinesin-coated tracks through engineered networks. *Lab on a Chip*, *4*(2), 83–86. doi:10.1039/b317059d

Collet, J.-P., Shuman, H., Ledger, R. E., Lee, S., & Weisel, J. W. (2005). The elasticity of an individual fibrin fiber in a clot. *Proceedings of the National Academy of Sciences of the United States of America*, *102*(26), 9133–7. doi:10.1073/pnas.0504120102

Deisseroth, K. (2012). Optogenetics. *Nature Methods*, 1–4. doi:10.1038/NMETH.F.324

Dennis, R. G., & Herr, H. (2005). Engineered Muscle Actuators : Cells and Tissues. In Y. Bar-Cohen (Ed.), *Biomimetics: Biologically Inspired Technologies* (1st ed., pp. 243–266). CRC Press.

Dennis, R. G., Kosnik, P. E., Gilbert, M. E., & Faulkner, J. A. (2001). Excitability and contractility of skeletal muscle engineered from primary cultures and cell lines Excitability and contractility of skeletal muscle engineered from primary cultures and cell lines. *Am J Physiol Cell Physiol*.

Dhariwala, B., Hunt, E., & Boland, T. (2004). Rapid Prototyping of Tissue-Engineering Constructs, Using Photopolymerizable Hydrogels and Stereolithography. *Tissue Engineering*, *10*(9/10), 1316–1323.

Duan, C., Ren, H., & Gao, S. (2010). Insulin-like growth factors (IGFs), IGF receptors, and IGF-binding proteins: roles in skeletal muscle growth and differentiation. *General and Comparative Endocrinology*, *167*(3), 344–51. doi:10.1016/j.ygcen.2010.04.009

Engler, A. J., Griffin, M. a, Sen, S., Bönnemann, C. G., Sweeney, H. L., & Discher, D. E. (2004). Myotubes differentiate optimally on substrates with tissue-like stiffness: pathological implications for soft or stiff microenvironments. *The Journal of cell biology*, *166*(6), 877–87. doi:10.1083/jcb.200405004

Entcheva, E. (2013). Cardiac Optogenetics. *American Journal of Physiology: Heart and Circulatory Physiology*, (631), 1–40. doi:10.1152/ajpheart.00432.2012

Feinberg, A. W., Feigel, A., Shevkoplyas, S. S., & Sheehy, S. (2007). Muscular Thin Films for Building. *Science*, *317*, 1366–1370.

Fenno, L., Yizhar, O., & Deisseroth, K. (2011). The development and application of optogenetics. *Annual Review of Neuroscience*, *34*, 389–412. doi:10.1146/annurev-neuro-061010-113817

Fisher, M. E., & Kolomeisky, A. B. (1999). The force exerted by a molecular motor. *Proceedings of the National Academy of Sciences of the United States of America*, *96*(12), 6597–602.

Florini, J. R., Ewton, D. Z., & Coolican, S. A. (1996). Growth hormone and the insulin-like growth factor system in myogenesis. *Endocrine Reviews*, *17*(5), 481–517.

Florini, J. R., Ewton, D. Z., & Roof, S. L. (1991). Insulin-like growth factor-I stimulates terminal myogenic differentiation by induction of myogenin gene expression. *Molecular endocrinology (Baltimore, Md.)*, *5*(5), 718–24.

Gerard, C., Forest, M. A., Beauregard, G., Skuk, D., & Tremblay, J. P. (2012). Fibrin gel improves the survival of transplanted myoblasts. *Cell Transplantation*, *21*, 127–37. doi:10.3727/096368911X576018

Gibson, I., Cheung, L. K., Chow, S. P., Cheung, W. L., Beh, S. L., Savalani, M., & Lee, S. H. (2006). The use of rapid prototyping to assist medical applications. *Rapid Prototyping Journal*, *12*(1), 53–58. doi:10.1108/13552540610637273

Goldspink, G., Scutt, A., Loughna, P. T., Wells, D. J., Jaenicke, T., & Gerlach, G. F. (1992). Gene expression in skeletal muscle in response to stretch and force generation. *American Journal of Physiology*, *262*, R356–363.

Han, B., Schwab, I. R., Madsen, T. K., & Isseroff, R. R. (2002). A Fibrin-based Bioengineered Ocular Surface With Human Corneal Epithelial Stem Cells. *Cornea*, *21*(5), 505–510. doi:10.1097/01.ICO.0000016343.19018.1D

Hecker, L., Khait, L., Radnoti, D., & Birla, R. (2008). Development of a microperfusion system for the culture of bioengineered heart muscle. *ASAIO Journal*, *54*(3), 284–94. doi:10.1097/MAT.0b013e31817432dc

Herr, H., & Dennis, R. G. (2004). A swimming robot actuated by living muscle tissue. *Journal of Neuroengineering and Rehabilitation*, *1*(1), 1–6. doi:10.1186/1743-0003-1-6

Hill, D. J., Crace, C. J., Fowler, L., Holder, a T., & Milner, R. D. (1984). Cultured fetal rat myoblasts release peptide growth factors which are immunologically and biologically similar to somatomedin. *Journal of Cellular Physiology*, *119*(3), 349–58. doi:10.1002/jcp.1041190314

Hinds, S., Bian, W., Dennis, R. G., & Bursac, N. (2011). The role of extracellular matrix composition in structure and function of bioengineered skeletal muscle. *Biomaterials*, *32*(14), 3575–83. doi:10.1016/j.biomaterials.2011.01.062

Hiratsuka, Y., Miyata, M., Tada, T., & Uyeda, T. Q. P. (2006). A microrotary motor powered by bacteria. *Proceedings of the National Academy of Sciences of the United States of America*, *103*(37), 13618–23. doi:10.1073/pnas.0604122103

Huang, C.-Y. C., Deitzer, M. a, & Cheung, H. S. (2007). Effects of fibrinolytic inhibitors on chondrogenesis of bone-marrow derived mesenchymal stem cells in fibrin gels. *Biomechanics and modeling in mechanobiology*, *6*, 5–11. doi:10.1007/s10237-006-0033-2

Huang, Y.-C., Dennis, R. G., Larkin, L., & Baar, K. (2005). Rapid formation of functional muscle in vitro using fibrin gels. *Journal of Applied Physiology*, *98*(2), 706–13. doi:10.1152/japplphysiol.00273.2004

Itoh, A. (2000). Motion control of protozoa for bio-MEMS. *IEEE/ASME Transactions on Mechatronics*, *5*(2), 181–188. doi:10.1109/3516.847091

Jacobs, P. F. (1992). *Rapid Prototyping and Manufacturing: Fundamentals of StereoLithography* (1st ed.). Society of Manufacturing Engineers.

Janmey, P. A., Winer, J. P., & Weisel, J. W. (2009). Fibrin gels and their clinical and bioengineering applications. *Journal of the Royal Society, Interface*, *6*(30), 1–10. doi:10.1098/rsif.2008.0327

Jeong, J. H., Chan, V., Cha, C., Zorlutuna, P., Dyck, C., Hsia, K. J., Bashir, R., et al. (2012). "Living" Microvascular Stamp for Patterning of Functional Neovessels; Orchestrated Control of Matrix Property and Geometry. *Advanced Materials*, *24*, 58–63. doi:10.1002/adma.201103207

Kamm, R. D., Nerem, R. M., & Hsia, K. J. (2010). Cells into Systems. *Mechanical Engineering*, 30–34.

Khodabukus, A., & Baar, K. (2009). Regulating Fibrinolysis to Engineer Skeletal Muscle from the C2C12 Cell Line. *Tissue Engineering: Part C*, *15*(3), 501–511.

Kidd, M. E., Shin, S., & Shea, L. D. (2012). Fibrin hydrogels for lentiviral gene delivery in vitro and in vivo. *Journal of Controlled Release*, *157*(1), 80–5. doi:10.1016/j.jconrel.2011.08.036

Kim, D.-H., Park, J., Suh, K. Y., Kim, P., Choi, S. K., Ryu, S., Park, S., et al. (2006). Fabrication of patterned micromuscles with high activity for powering biohybrid microdevices. *Sensors and Actuators B: Chemical*, *117*(2), 391–400. doi:10.1016/j.snb.2005.11.051

Kim, J., Park, J., Yang, S., Baek, J., Kim, B., Lee, S. H., Yoon, E.-S., et al. (2007). Establishment of a fabrication method for a long-term actuated hybrid cell robot. *Lab on a Chip*, *7*(11), 1504–8. doi:10.1039/b705367c

Koch, S., Flanagan, T. C., Sachweh, J. S., Tanios, F., Schnoering, H., Deichmann, T., Ellä, V., et al. (2010). Fibrin-polylactide-based tissue-engineered vascular graft in the arterial circulation. *Biomaterials*, *31*(17), 4731–9. doi:10.1016/j.biomaterials.2010.02.051

Koning, M., Harmsen, M. C., Luyn, M. J. A. Van, & Werker, P. M. N. (2009). Current opportunities and challenges in skeletal muscle tissue engineering, (July), 407–415. doi:10.1002/term

Kosnik, P. E., Faulkner, J. A., & Dennis, R. G. (2001). Functional Development of Engineered Skeletal Muscle from Adult and Neonatal Rats. *Tissue Engineering*, *7*(5), 573–584.

Kupcsik, L., Alini, M., & Stoddart, M. J. (2009). Epsilon-aminocaproic acid is a useful fibrin degradation inhibitor for cartilage tissue engineering. *Tissue Engineering: Part A*, *15*(8), 2309–13. doi:10.1089/ten.tea.2008.0400

Lam, M. T., Huang, Y.-C., Birla, R. K., & Takayama, S. (2009). Microfeature guided skeletal muscle tissue engineering for highly organized 3-dimensional free-standing constructs. *Biomaterials*, *30*(6), 1150–5. doi:10.1016/j.biomaterials.2008.11.014

Lei, P., Padmashali, R. M., & Andreadis, S. T. (2009). Cell-controlled and spatially arrayed gene delivery from fibrin hydrogels. *Biomaterials*, *30*(22), 3790–9. doi:10.1016/j.biomaterials.2009.03.049

Li, M., Dickinson, C. E., Finkelstein, E. B., Neville, C. M., & Sundback, C. A. (2011). The Role of Fibroblasts in Self-Assembled Skeletal Muscle. *Tissue Engineering: Part A*, *17*(21-22), 2641–2650. doi:10.1089/ten.tea.2010.0700

Liao, H., & Zhou, G.-Q. (2009). Development and progress of engineering of skeletal muscle tissue. *Tissue engineering. Part B, Reviews*, *15*(3), 319–31. doi:10.1089/ten.teb.2009.0092

Lieber, R. L. (2002). *Skeletal Muscle Structure, Function, & Plasticity*. (T. Julet, Ed.) (2nd ed.). Baltimore, MD: Lippincott Williams & Wilkins.

Liu, W., Jawerth, L. M., Sparks, E. A., Falvo, M. R., Hantgan, R. R., Superfine, R., Lord, S. T., et al. (2006). Fibrin fibers have extraordinary extensibility and elasticity. *Science*, *313*(5787), 634. doi:10.1126/science.1127317

Lu, Y., Mapili, G., Suhali, G., Chen, S., & Roy, K. (2006). A digital micro-mirror device-based system for the microfabrication of complex, spatially patterned tissue engineering scaffolds. *Journal of Biomedical Materials Research: Part A*, *77*(2), 396–405. doi:10.1002/jbm.a.30601

Manning, B. D., & Cantley, L. C. (2007). AKT/PKB signaling: navigating downstream. *Cell*, *129*(7), 1261–74. doi:10.1016/j.cell.2007.06.009

Marieb, E. N. (Ed.). (2006). Muscles and Muscle Tissue. *Essentials of Human Anatomy and Physiology* (8th ed., pp. 279–326). Pearson Benjamin Cummings.

Melchels, F. P. W., Feijen, J., & Grijpma, D. W. (2010). A review on stereolithography and its applications in biomedical engineering. *Biomaterials*, *31*(24), 6121–30.

Morishima, K., Tanaka, Y., Ebara, M., Shimizu, T., Kikuchi, A., Yamato, M., Okano, T., et al. (2006). Demonstration of a bio-microactuator powered by cultured cardiomyocytes coupled to hydrogel micropillars. *Sensors and Actuators B: Chemical*, *119*(1), 345–350. doi:10.1016/j.snb.2005.11.063

Nagamine, K., Kawashima, T., Sekine, S., Ido, Y., Kanzaki, M., & Nishizawa, M. (2011). Spatiotemporally controlled contraction of micropatterned skeletal muscle cells on a hydrogel sheet. *Lab on a chip*, *11*(3), 513–7. doi:10.1039/c0lc00364f

Nawroth, J. C., Lee, H., Feinberg, A. W., Ripplinger, C. M., McCain, M. L., Grosberg, A., Dabiri, J. O., et al. (2012). A tissue-engineered jellyfish with biomimetic propulsion. *Nature Biotechnology*, *30*(8), 792–797. doi:10.1038/nbt.2269

Noji, H., Yasuda, R., Yoshida, M., & Kinosita, K. J. (1997). Direct observation of the rotation of F1-ATPase. *Nature*, *386*(6622), 299–302.

Ontell, M., & Kozeka, K. (1984). The organogenesis of murine striated muscle: a cytoarchitectural study. *The American Journal of Anatomy*, *171*(2), 133–148. doi:10.1002/aja.1001710202

Pastrana, E. (2010). Optogenetics: controlling cell function with light. *Nature Methods*, *8*(1), 24–25. doi:10.1038/nmeth.f.323

Peltola, S., Melchels, F. P. W., Grijpma, D. W., & Kellomäki, M. (2008). A Review of Rapid Prototyping Techniques for Tissue Engineering Purposes. *Annals of Medicine*, *40*(4), 268–280.

Piccolino, M. (2000). Biological machines: from mills to molecules. *Nature Reviews: Molecular Cell Biology*, *1*(2), 149–153. doi:10.1038/35040097

Pilarek, M., Neubauer, P., & Marx, U. (2011). Biological cardio-micro-pumps for microbioreactors and analytical micro-systems. *Sensors & Actuators: B. Chemical*, *156*(2), 517–526. doi:10.1016/j.snb.2011.02.014

Powell, C. a, Smiley, B. L., Mills, J., & Vandenburgh, H. H. (2002). Mechanical stimulation improves tissue-engineered human skeletal muscle. *American Journal of Physiology - Cell Physiology*, *283*(5), C1557–1565. doi:10.1152/ajpcell.00595.2001

Prentice, C. R. M. (1980). Basis of antifibrinolytic therapy. *Journal of Clinical Pathology*, *14*, 35–40.

Rein, M. L., & Deussing, J. M. (2012). The optogenetic (r)evolution. *Molecular Genetics and Genomics*, *287*(2), 95–109. doi:10.1007/s00438-011-0663-7

Ren, H., Yin, P., & Duan, C. (2008). IGFBP-5 regulates muscle cell differentiation by binding to IGF-II and switching on the IGF-II auto-regulation loop. *The Journal of Cell Biology*, *182*(5), 979–91. doi:10.1083/jcb.200712110

Robinson, P. S., Johnson, S. L., Evans, M. C., Barocas, V. H., & Tranquillo, R. T. (2008). Functional tissue-engineered valves from cell-remodeled fibrin with commissural alignment of cell-produced collagen. *Tissue engineering. Part A*, *14*(1), 83–95. doi:10.1089/ten.a.2007.0148

Ryan, E. A., Mockros, L. F., Weisel, J. W., & Lorand, L. (1999). Structural origins of fibrin clot rheology. *Biophysical Journal*, *77*(5), 2813–26.

Sakar, M. S., Neal, D., Boudou, T., Borochin, M. a, Li, Y., Weiss, R., Kamm, R. D., et al. (2012). Formation and optogenetic control of engineered 3D skeletal muscle bioactuators. *Lab on a Chip*, *12*(23). doi:10.1039/c2lc40338b

Sakar, M. S., Neal, D., Boudou, T., Borochin, M. A., Weiss, R., Kamm, R. D., Chen, C. S., et al. (2012). Formation and Optogenetic Control of Engineered 3D Skeletal Muscle Bioactuators - Electronic Supplementary Information.

Salmon, W. D. J., & Daughaday, W. H. (1957). A hormonally controlled serum factor which stimulates sulfate incorporation by cartilage in vitro. *J Lab Clin Med*, *49*(6), 825–36.

Shansky, J., Creswick, B., Lee, P., Wang, X., & Vandenburgh, H. H. (2006). Paracrine release of insulin-like growth factor 1 from a bioengineered tissue stimulates skeletal muscle growth in vitro. *Tissue Engineering*, *12*(7), 1833–41. doi:10.1089/ten.2006.12.1833

Soong, R. K., Bachand, G. D., Neves, H. P., Olkhovets, A. G., Craighead, H. G., & Montemagno, C. D. (2000). Powering an Inorganic Nanodevice with a Biomolecular Motor. *Science*, *290*, 1555–1558. doi:10.1126/science.290.5496.1555

Stewart, C. E., James, P. L., Fant, M. E., & Rotwein, P. (1996). Overexpression of insulin-like growth factor-II induces accelerated myoblast differentiation. *Journal of Cellular Physiology*, *169*(1), 23–32. doi:10.1002/(SICI)1097-4652(199610)169:1<23::AID-JCP3>3.0.CO;2-G

Tanaka, Y., Morishima, K., Shimizu, T., Kikuchi, A., Yamato, M., Okano, T., & Kitamori, T. (2006). An actuated pump on-chip powered by cultured cardiomyocytes. *Lab on a chip*, *6*(3), 362–8. doi:10.1039/b515149j

Tanaka, Y., Sato, K., Shimizu, T., Yamato, M., Okano, T., & Kitamori, T. (2007a). Biological cells on microchips: new technologies and applications. *Biosensors and Bioelectronics*, *23*(4), 449–58. doi:10.1016/j.bios.2007.08.006

Tanaka, Y., Sato, K., Shimizu, T., Yamato, M., Okano, T., & Kitamori, T. (2007b). A micro-spherical heart pump powered by cultured cardiomyocytes. *Lab on a chip*, *7*(2), 207–12. doi:10.1039/b612082b

Tung, S., & Kim, J. W. (2006). Microscale Hybrid Devices Powered by Biological Flagellar Motors. *IEEE Transactions on Automation Science and Engineering*, *3*(3), 260–263.

Valentovic, M. (2007). *Aminocaproic Acid* (pp. 1–5). Huntington, USA.

Vandenburgh, H. H., Karlisch, P., Shansky, J., & Feldstein, R. (1991). Insulin and IGF-I induce pronounced hypertrophy of skeletal myofibers in tissue culture. *American Journal of Physiology - Cell Physiology*, *260*(3), C475–484.

Watanabe, H. C., Welke, K., Schneider, F., Tsunoda, S., Zhang, F., Deisseroth, K., Hegemann, P., et al. (2012). Structural model of channelrhodopsin. *The Journal of Biological Chemistry*, *287*(10), 7456–66. doi:10.1074/jbc.M111.320309

Watras, J. M. (2008). Muscle. In B. M. Koeppen & B. A. Stanton (Eds.), *Berne & Levy Physiology* (6th ed., pp. 233–267). Philadelphia, PA: Mosby Elsevier.

Weibel, D. B., Garstecki, P., Ryan, D., DiLuzio, W. R., Mayer, M., Seto, J. E., & Whitesides, G. M. (2005). Microoxen: microorganisms to move microscale loads. *Proceedings of the National Academy of Sciences of the United States of America*, *102*(34), 11963–7. doi:10.1073/pnas.0505481102

Weisel, J. W. (2004). The mechanical properties of fibrin for basic scientists and clinicians. *Biophysical chemistry*, *112*(2-3), 267–76. doi:10.1016/j.bpc.2004.07.029

Weisel, J. W. (2005). Fibrinogen and Fibrin. In D. A. D. Parry & J. M. Squire (Eds.), *Advances in Protein Chemistry* (Vol. 70, pp. 247–299). Academic Press. doi:10.1016/S0065-3233(04)70008-X

Weisel, J. W. (2007). Structure of fibrin: impact on clot stability. *Thrombosis and Haemostasis*, *5*(Suppl. 1), 116–24. doi:10.1111/j.1538-7836.2007.02504.x

Wolberg, A. S. (2007). Thrombin generation and fibrin clot structure. *Blood reviews*, *21*(3), 131–42. doi:10.1016/j.blre.2006.11.001

Xi, J., Schmidt, J. J., & Montemagno, C. D. (2005). Self-assembled microdevices driven by muscle. *Nature materials*, *4*(2), 180–4. doi:10.1038/nmat1308

Zammit, P. S., Partridge, T. a, & Yablonka-Reuveni, Z. (2006). The skeletal muscle satellite cell: the stem cell that came in from the cold. *The Journal of Histochemistry and Cytochemistry*, *54*(11), 1177–91. doi:10.1369/jhc.6R6995.2006

Zhang, F., Vierock, J., Yizhar, O., Fenno, L., Tsunoda, S., Kianianmomeni, A., Prigge, M., et al. (2011). The microbial opsin family of optogenetic tools. *Cell*, *147*(7), 1446–57. doi:10.1016/j.cell.2011.12.004

Zhang, F., Wang, L., Boyden, E. S., & Deisseroth, K. (2006). Channelrhodopsin-2 and optical control of excitable cells. *Nature Methods*, *3*(10), 785–792. doi:10.1038/NMETH936

Zhang, F., Wang, L.-P., Brauner, M., Liewald, J. F., Kay, K., Watzke, N., Wood, P. G., et al. (2007). Multimodal fast optical interrogation of neural circuitry. *Nature*, *446*(7136), 633–9. doi:10.1038/nature05744

Zorlutuna, P., Jeong, J. H., Kong, H., & Bashir, R. (2011). Stereolithography-Based Hydrogel Microenvironments to Examine Cellular Interactions. *Advanced Functional Materials*, *21*, 3642–3651. doi:10.1002/adfm.201101023